This preprint article has been submitted to Quaternaly Journal of the Royal Meteorological Society [Website] on June 22, 2023. It is currently peer-reviewed.

ORIGINAL ARTICLE
Journal Section

Coherent subsiding structures in large eddy simulations of atmospheric boundary layers

Florent Brient[1] | Fleur Couvreux[2] | Catherine Rio[2] | Rachel Honnert[2]

[1]LMD/IPSL, Sorbonne Université, Paris, France
[2]CNRM, Université de Toulouse, Météo-France, CNRS, Toulouse, France

Correspondence
Florent Brient, LMD/IPSL, Sorbonne Université, Paris, France
Email: florent.brient@lmd.ipsl.fr

Funding information
French ANR, Grants Numbers: HIGH-TUNE ANR-16-CE01-0010 and MOBYDYC ANR-22-CE01-0005

Coherent structures are characterized in high-resolution simulations of three atmospheric boundary layers: dry convection, marine cumulus, and stratocumulus. Based on radioactive-decaying tracers emitted at different altitudes (surface, top of well-mixed layer, and cloud top), a object-oriented methodology allows individual characterization of coherent tridimensional plumes within the flow.

Each boundary layer show updraft structures surrounded by subsiding shells that have similar thermodynamical characteristics. Well-mixed downdrafts are located relatively close to updrafts and entrain dry, warm air from the free troposphere. Identified in all boundary layers, these subsiding structures are triggered by air mass convergence linked to updrafts' divergence and are thus part of an overturning circulation in well-mixed layers. Close to the surface, downdrafts' divergence constrain updrafts' locations and thus shape a mesoscale cellular organisation with cell sizes scaling the boundary-layer height.

Active cumulus formation does not strongly perturb the spatial organisation of the sub-cloud well-mixed layer. Similarly, the stratocumulus-topped boundary layers shows similar overturning circulation despite having condensation and cloud-radiation diabatic effects. However, the daytime decoupling in stratocumulus layers reduces the ability of updrafts to reach the boundary-layer top (and downdrafts to reach the surface) that finally influence the visible mesoscale organisation of stratocumulus cells.

Since well-mixed downdrafts contribute to a significant part of resolved flux of heat and moisture, our results suggest that downdraft properties in well mixed layers should be represented at the subgrid scale in climate models through non-local mass-flux parameterizations.

KEYWORDS
atmospheric boundary layer, clouds, coherent structures, downdraft, large-eddy simulation, mesoscale organisation, Rayleigh-Bénard convection, parameterization

1 | INTRODUCTION

The atmospheric boundary layer (BL) plays an important role in the Earth's energetic system. Located over the first kilometers of the atmosphere, it controls exchanges of heat, moisture and momentum between the surface and the free atmosphere. Processes occurring within this relatively thin layer drive the formation of low clouds, which significantly influence the Earth's radiative budget. By the formation of cumuliform clouds, BL processes are also of major importance for the redistribution of available heat and moisture. It is thus understandable that potential biases in simulating the atmospheric BL in large-scale models and numerical weather prediction would induce errors in reproducing various aspects of the climate system. Improving physical sub-grid assumptions that aim to represent the complexity and variability of BLs remains a difficult yet essential challenge for the climate science.

The convective boundary layer is one of the most common BL regime, over which surface fluxes drive convective mixing. It can be decomposed in a shallow surface layer, a well-mixed layer, and a thin entrainment zone around the capping inversion that controls exchanges with the free troposphere. In the mixed layer, surface-driven positively-buoyant coherent vertical structures (i.e. updrafts or plumes) control turbulent mixing by carrying heterogeneities in heat, moisture, and momentum upward and thus maintain the layer well homogeneized. Most current BL parameterizations represent BL transport through a combination between local eddy diffusivity and non-local mass fluxes (*Hourdin et al.*, 2002; *Siebesma et al.*, 2007). Mass-flux approaches usually assume that convective plumes are thin and surrounded by a wide zone of slow (compensating) subsidence within a model grid. This approach has successfully improved our ability to represent some important boundary-layer processes (e.g. *Rio and Hourdin*, 2008), even if persistent model errors and disagreements still remain in current climate models (*Richter*, 2015).

Conversely, downward motions receive much less attention and are rarely represented in current climate models. BL coherent downward motions are often separated in, at least, three main categories:

- **Subsiding shells**. Firstly observed by *Jonas* (1990), subsiding shells are thin layers surrounding condensed cumuliform clouds. They are linked to lateral detrainment, and likely triggered by local evaporation that generate negatively-buoyant sinking air parcels (*Heus and Jonker*, 2008). Conversely, mechanical triggering associated with the vortical structure of cloud thermals has also been highlighted (*Sherwood et al.*, 2013; *Romps and Charn*, 2015;

Park et al., 2017). Strength of subsiding shells thus depend on updraft convective mixing and diabatic forcing.

- **Stratocumulus downdrafts** In well-mixed stratocumulus-top BLs, downward structures consist in air parcels entrained from the free troposphere to the boundary layer, which become negatively buoyant by radiative and evaporative cooling of liquid water and therefore accelerate (*Wood*, 2012). The relative strength of downdrafts is influenced by various characteristics, such as BL decoupling (*Bretherton and Wyant*, 1997), aerosol concentration (*Feingold et al.*, 2010), or precipitation (*Stevens et al.*, 1998). Drivers of downward motions are not yet clearly identified, as they either are slaved to the mesoscale overturning convective circulation (*Nicholls*, 1989; *Zhou and Bretherton*, 2019a,b), or triggered by local buoyancy reversal processes (*Deardorff*, 1980; *Randall*, 1980). *Yamaguchi and Randall* (2012) suggest that both may act, as small-scale cloud-top mixing between warm, dry tropospheric parcels and moist, cooler BL parcels trigger subsiding plumes, which are then carried and organized by large-scale converging flows atop the well-mixed layer (cellular pattern). These downdrafts carry a significant part of heat and moisture (*Davini et al.*, 2017; *Chinita et al.*, 2018; *Brient et al.*, 2019).
- **Dry tongues**. In the clear-sky continental convective BL, coherent downdrafts carry dry and warm air from layers above the mixed layer (*Schmidt and Schumann*, 1989; *Mahrt*, 1991). Due to their conic form, they can be named dry tongues (*Couvreux et al.*, 2005, 2007). Located around upward convective plumes, dry tongues might be a part of some open-celled clear-sky mesoscale organisation (*Bennett et al.*, 2010). Observations confirm the existence of dry tongues either with or in the absence of cloudiness (*Lareau et al.*, 2018; *Lareau*, 2020). In a (sub-cloud) convective BL, clear-sky downdrafts might thus be triggered by dynamical forcing.

Recent studies seek to improve the representation of downward coherent structures in convective BLs simulated by climate models. For instance, *Suselj et al.* (2019) suggest a sub-grid mass-flux representation of subsiding shells triggered by the evaporation of precipitation detrained from cloudy updrafts. Similar assumptions can be used for representing downdrafts in stratocumulus-topped BL (*Han and Bretherton*, 2019; *Wu et al.*, 2020). They have showed that downdrafts only contribute weakly to heat and moisture vertical transport relative to the updraft contribution. This is in disagreement with modeling studies that suggest significant downdraft fluxes (e.g. *Brient et al.*, 2019).

One issue is that such parameterizations of downdrafts are based on diabatic triggering (solar heating, longwave cooling and evaporation/condensation effects), which will not allow clear-sky downdrafts to be represented. The existence of coherent downdrafts in different convective BLs challenges both the assumption of compensating subsidence in the usual convective plume parameterizations, and the diabatic view for downdraft triggering. Furthermore, downdraft structures seem to be embedded in mesoscale organisations, which question the ability climate models have to represent such spatial organisation at the sub-grid scale. This calls for revisiting our understanding of physical processes associated with coherent downward motions in order to provide an unified approach for modeling downdrafts across various boundary layers.

In that purpose, a first step consists in identifying coherent structures in different boundary layers. Large eddy simulations (LES) have often been used to provide insights into convective structures within boundary layers, with a specific description of coherent downward motions in clear-sky downdrafts (*Couvreux et al.*, 2005, 2007), subsiding shells (*Heus and Jonker*, 2008; *Park et al.*, 2016) and cloud-top entraining downdrafts (*Davini et al.*, 2017; *Chinita et al.*, 2018; *Brient et al.*, 2019). However, differences in resolution, model parameterizations, and methods for identifying structures reduce the credibility of intercomparing analysis. In order to reduce this uncertainty, one must use a common framework. The community now offers the opportunity to simulate a large number of boundary layers thanks to numerous intercomparison studies that provide large-scale forcing and boundary conditions. If one applies a common methodology to extract coherent structures, the description of their similarities and differences would likely be more rigorous, and the underlying analysis more robust. In that aim, we apply the object-oriented methodology described in

Brient et al. (2019) to three distinct boundary-layer LES in order to extract and analyze downward coherent structures in an ensemble of boundary-layer conditions.

In this paper, we first describe the three BL LES and the object-oriented methodology used for identifying coherent structures (section 2). Characteristics of coherent structures are analyzed, with a focus on their relative contributions to turbulent fluxes (section 3). Origins of downdrafts are then investigated in clear-sky and cloud-topped convective boundary layers (section 4). Links between coherent structures and the mesoscale organisation, and how they might be represented in climate models are discussed in section 5.

2 | COHERENT STRUCTURES IN LARGE-EDDY SIMULATIONS OF BOUNDARY LAYERS

2.1 | Common setup for simulating boundary layers

We use the Meso-NH model version 5.4.2 (*Lafore et al.*, 1998; *Lac et al.*, 2018) to reproduce three different BL regimes: the IHOP clear-sky convective BL (*Couvreux et al.*, 2005), the BOMEX marine cumulus (*Siebesma et al.*, 2007) and the FIRE stratocumulus (*Duynkerke et al.*, 2004). Simulations focus on warm conditions, i.e. related to liquid clouds, over both oceanic and land surfaces.

In an attempt to compare simulations across each other, we slightly modify the original formalisms of IHOP and BOMEX to a common 12.8x12.8 km^2 domain with 25m horizontal resolution. The vertical resolution is 25m within the boundary layer (and larger above for IHOP). However, the FIRE simulation is simulated over a larger horizontal domain (25.6x25.6 km^2) with coarser horizontal resolution (50m) in order to represent the extensive size of the mesoscale cloud organization. A refined vertical resolution (10m) is also applied to represent small-scale eddies atop the cloud layer. Finally, the common time step is set at 1s. Surface and large-scale forcing follow the original setup. Description of simulations and parameterizations are described in Appendix A.

2.2 | Object-oriented coherent structures

In order to identify coherent structures within boundary layers, we use the methodology described in *Brient et al.* (2019). Based on *Couvreux et al.* (2010), objects are defined from passive tracers emitted either at the surface or at the cloud top. We construct objects from anomalies of their concentration relative to horizontal mean. First, we define a conditional sampling (CS) that select grid boxes containing sufficiently large anomalies of tracer concentrations. Second, objects are defined as ensembles of contiguous selected grid boxes built in a three-dimensional space. Here "contiguous" means sharing either a face, an edge or a corner, i.e. 26-connectivity. Third, identified objects with a smaller volume than V_{min} are filtered out.

However, several parts of the original framework have been modified:

- Associated with tracers emitted at the surface (s_1) and above the domain-mean cloud top (s_2), a third passive tracer s_3 is emitted one layer above the domain-mean cloud base. Sub-cloud structures are defined through s_3 tracer anomalies only below the layer (Table 1).
- For clear-sky simulations, s_3 is emitted above the boundary-layer top, which is defined as the first altitude where the domain-mean virtual potential temperature $\overline{\theta_v}$ becomes larger than the integral of $\overline{\theta_v}$ below plus an offset fixed at 0.25K (*Couvreux et al.*, 2007). As this tracer is *entrained* in the well-mixed clear-sky layer, we will refer objects defined through this tracer as s_3 objects (Table 1).

TABLE 1 Object definition of coherent structures

	Object name	Color	Symbol	CS_s	CS_w
1	updraft	red	//	surface-emitted s_1	w>0
2	subsiding shells	purple	·	surface-emitted s_1	w<0
3	cloud-top downdraft	blue	\\	cloud-top s_2	w<0
4	well-mixed downdraft	green	+	cloud base or boundary-layer top s_3	w<0

- A double condition is applied for distinguishing the core of the updraft plume (positive vertical velocity w>0) from subsiding shells (w<0), and to reduce effects of small-scale turbulence.
- Because IHOP and BOMEX have smaller domains and convective structures, we fix V_{min}=2 10^{-2} km^3 for the three simulations. This volume is 12.5 times smaller than the threshold used in *Brient et al.* (2019) (i.e., 0.25 km^3).

The selection of grid cells (x, y, z) satisfying the total conditional sampling CS corresponds to both a selection based on tracer anomalies CS$_s$ and on vertical velocity CS$_w$. The CS$_s$ part is defined as

$$\Big\{(x, y, z) \in \mathrm{CS}_s \quad | \quad s'(x, y, z) > \sigma(z)\Big\} \tag{1}$$

with s' the tracer anomaly concentration relative to the horizontal mean ($\bar{s}$) and $\sigma(z)$ the horizontal-mean threshold at altitude z, defined as :

$$\begin{aligned} \sigma(z) &= m \cdot \max(\sigma_s(z), \sigma_{min}(z)) && (2) \\ \text{with } \sigma_{min}(z) &= L \cdot \frac{\gamma}{z - z_1} \int_{z_1}^{z} \sigma_s(z) dz && (3) \end{aligned}$$

with $\sigma_s(z)$ being the standard deviation of the tracer concentration s at altitude z, and with L=1 for s_1 and L=-1 for s_2 and s_3. The minimal threshold σ_{min} is used to under-represent layers with low tracer concentrations and thus weak standard deviation (i.e. filtering out the non-turbulent free troposphere for s_1 and the lowest layers for s_2 and s_3). Its efficiency is related to the γ parameter, which is fixed at γ=0.005 (0.05 in *Brient et al.* (2019)). For the s_1 bottom-up integration, we choose z_1 as the surface. For s_2 and s_3 top-down integration, z_1 is fixed at 2 layers above the level with maximum domain-mean tracer concentration. The scaling factor m used in equation 2 is a tunable parameter that quantifies the strength of the conditional sampling. Here m=1.

While CS$_s$ does not use flow characteristics, the second conditional sampling CS$_w$ selects grid boxes with positive or negative vertical velocities. Finally, the full conditional sampling CS selects grid cells satisfying together CS$_s$ and CS$_w$ (CS$_s$ ∩ CS$_w$). Table 1 summarize object definitions and captions used in the following figures.

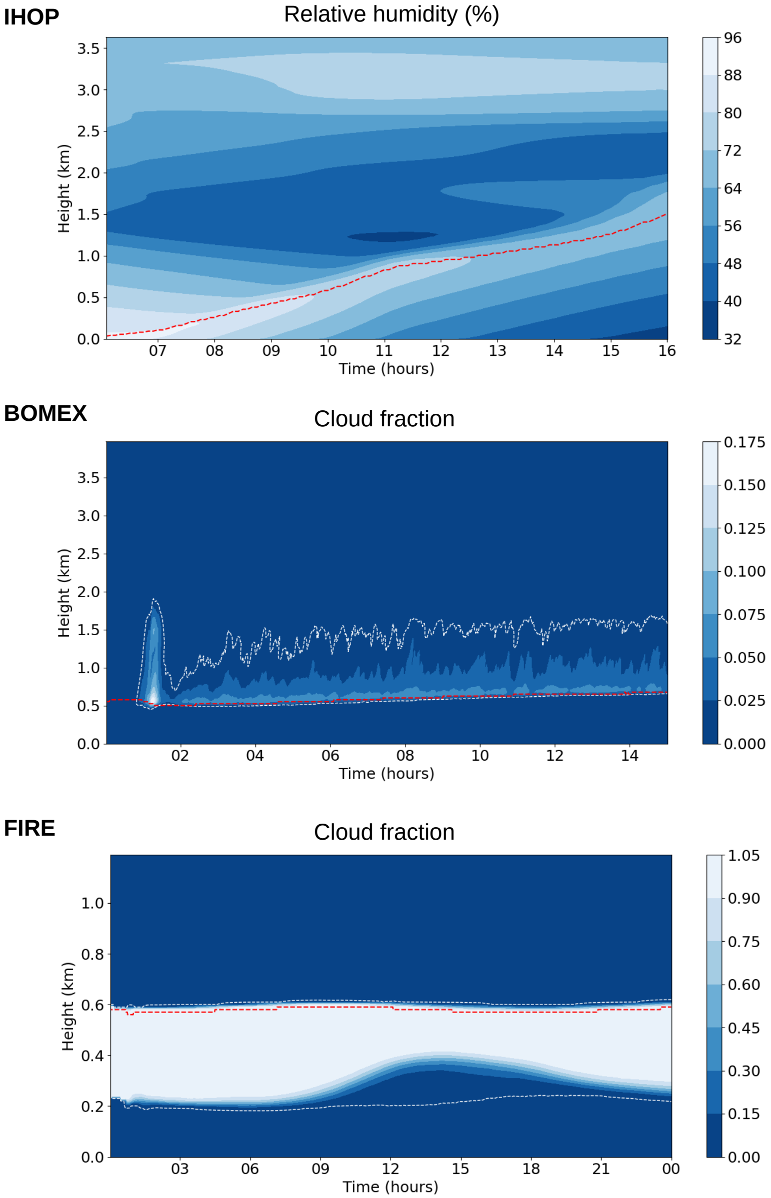

FIGURE 1 Temporal evolution of the domain-mean relative humidity for IHOP (top) and cloud fraction for BOMEX and FIRE (middle and bottom respectively). The 1% cloud fraction contours and the mixed layer depth z_i are plotted as white and red dashed lines respectively. For FIRE, note that the vertical size of the domain is 4 times smaller and the color scale is different. Hours are local time.

TABLE 2 Domain-mean boundary-layer characteristics (m): depth of the boundary layer z_i, Lifting Condensation Level (LCL), Level of Free Convection (LFC), Level of Neutral Buoyancy (LNB), cloud base and cloud top.

	time	z_i	LCL	LFC	LNB	cloud base	cloud top
IHOP	12h	955	1405	2130	2230	-	-
BOMEX	8h	625	575	675	1700	600	1725
BOMEX No Winds	8h	600	550	600	1650	575	1625
FIRE (day)	12h	600	200	250	600	230	610
FIRE (night)	21h	590	260	280	590	260	600

3 | CHARACTERIZATION OF COHERENT STRUCTURES IN BOUNDARY-LAYER SIMULATIONS

3.1 | Overview

Figure 1 shows the temporal evolution of cloud fraction or relative humidity. The IHOP dry convective BL shows a diurnal deepening of the boundary layer from the early morning to early afternoon associated with the increase of surface fluxes. The convective mixing dries the BL, which deepens at a constant rate throughout the day until reaching 1.5 km depth. The BOMEX marine BL is stable in time with some spin-up period of around 2 hours. The cloudy BL is around 1.5 km deep, with maximum cloud fraction close to the domain-mean cloud base (z=0.5-0.6 km). The sub-cloud layer slightly deepens in time. The FIRE stratocumulus BL shows a thick cloud layer between 0.2 and 0.6 km, that thins during daytime (between 10h and 20h). At that time period, the domain-mean cloud fraction increases more slowly with the altitude.

Depth of the well-mixed layer z_i is also shown in Figure 1. z_i is defined as the altitude where the liquid potential temperature θ_l stop being well-mixed, i.e. where θ_l becomes greater than the density-weighted mean $\overline{\theta_l}$(z) of the levels below by a certain threshold ϵ ($|\theta_l(z)-\overline{\theta_l}(z)| \geq \epsilon$). Here, we fix ϵ=0.25 K. Values of z_i for specific time are listed in Table 2.

Figure 2 shows spatial patterns of relative humidity at z_i. The clear-sky BL organizes in cells of relative humidity of around 2 km diameter, with narrow bands of weak humidity surrounding them. Anomalies of vertical velocity are mostly located in their centers but do not show sign of spatial organisation (not shown). The cumulus BL shows no specific organisation in space, but large regions of negative relative humidity anomalies and narrow saturated structures (clouds) of around 500 m diameter. Finally, the stratocumulus-topped BL organizes in elongated cells of around 15 km at nighttime. During daytime, stratocumulus are organized in cells of around 10 km diameter (see section 4.2).

3.2 | Object characteristics

3.2.1 | The convective clear-sky boundary layer

Figure 3 shows the domain-mean areal fraction of coherent structures and a cross section to highlight positions of structures. For IHOP, coherent structures cover 24.6% of the boundary layer (Table 3), distributed almost equally over almost all altitudes. While updrafts and downdrafts extend uniformly, subsiding shells are only located over a thin layer of around 400m depth at the BL top with maximum coverage of 5%. Cross section shows that updrafts and downdrafts

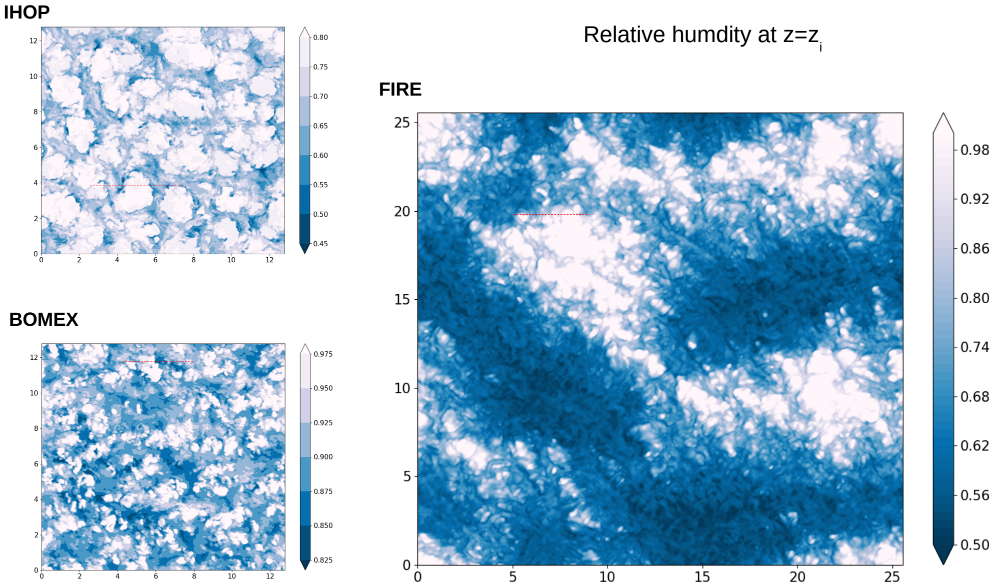

FIGURE 2 Relative humidity at the top of the boundary layer (z=z$_i$) for IHOP (t=12h), BOMEX (t=8h) and FIRE (t=21h). Red dashed lines are segments of cross sections shown in figure 3. The relative size of figures approximately scales with the domain size of simulations. Color bars are different between simulations to highlight spatial organisations.

are separated by around 1 km, which approximately scales the cell radius shown in Figure 2. Subsiding shells are located atop updraft plumes with weak vertical extension[1]. The existence of large areas with no coherent convective structures suggests that the downdrafts are not compensating downward motions covering the complementary area of updraft cover. While updrafts and subsiding shells have positive moisture anomalies, well-mixed downdrafts are drier than the environment.

The domain-averaged object features are shown in Figure 4. Updrafts show bottom-heavy vertical wind profile that maximize around $0.4z_i$, and warmer/colder air than the environment below/above $0.8z_i$. Subsiding shells have similar moisture and temperature characteristics than updrafts, confirming that they are the returning parts of updrafts (weak lateral detrainment). Downdrafts have a bottom-heavy negative vertical velocity profile maximizing at $0.3z_i$ –suggesting downward acceleration of air parcels– are drier than the environment and warmer around z_i (colder below). Downdrafts are initiated around $1.1z_i$ with no vertical velocity, positive buoyancy and convergence of air masses, which suggest mechanistic forcing for triggering these subsiding structures. In the well-mixed layer, buoyancy decreases and becomes positive around 0.6 z_i. Below $0.4z_i$, downdrafts start diverging while updrafts show large convergence (especially close to the surface). Note that objects' divergence becomes null at the altitude where vertical velocity maximizes.

---

[1] Since turbulent shells are mostly related to the returning branches of upward plumes (both defined through radioactive-decaying surface-emitted s_1 tracer concentration), their coverage might be underestimated when getting closer to the surface.

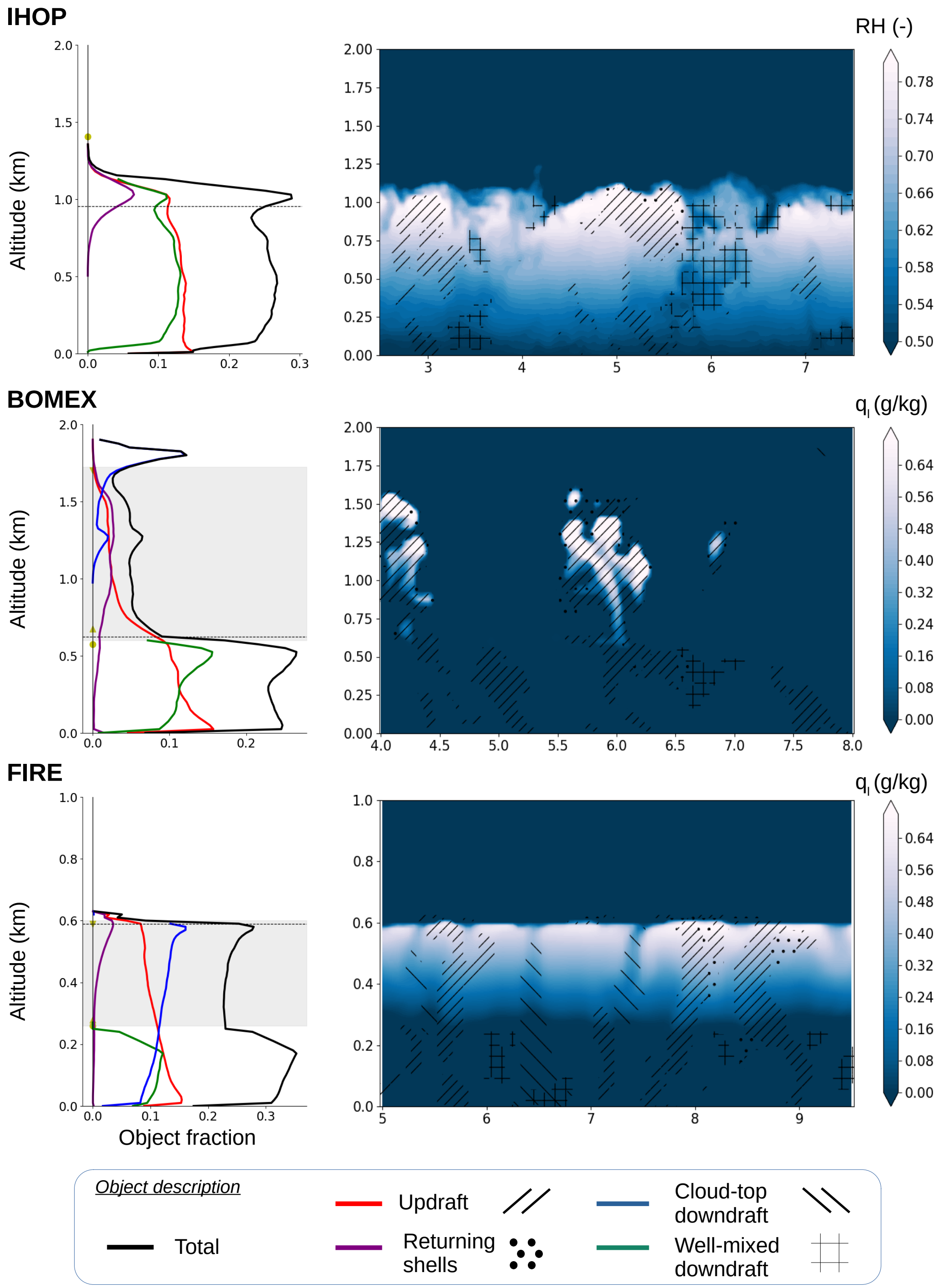

FIGURE 3 Object characteristics for the 3 boundary-layer simulations (IHOP, BOMEX, FIRE). Left panels show the domain-mean object coverage and right panels show cross sections for relative humidity (IHOP) and liquid water content (BOMEX, FIRE) over segments shown in Figure 2. Coverage by updrafts, subsiding shells, cloud-top downdrafts and well-mixed downdrafts are represented as red (//), purple (·), blue (\\), and green (+) and colors (symbols) for the domain-mean profile (cross section) respectively. On vertical profiles (left panel), the yellow circle represents the domain-mean Lifting Condensation Level (LCL), upside and downside yellow triangles are the Level of Free Convection (LFC) and Level of Neutral Buoyancy (LNB) respectively, and the horizontal dotted line represents the well-mixed layer top z_i defined with the θ_l method (see main text).The grey area represent the cloud layer defined between the domain-mean cloud top and cloud base (if available).

TABLE 3 Object characteristics averaged below $1.1z_i$ for IHOP (altitude of maximum tracer concentration), and below the domain-mean cloud top for FIRE and BOMEX. The 'sb' index for BOMEX corresponds to averaged values only below z_i (Table 2). For each object type, coverage, number of objects, and relative contribution to heat and humidity transport are shown. 'All' are values averaged over grid points satisfying at least one conditional sampling.

	Type	Cover (%)		Number		$F_i\,[\theta_l]$ (%)		$F_i\,[q_t]$ (%)	
IHOP	upd	12.6		10		70.8		62.6	
[t=12h]	sub	1.1		29		4.04		7.32	
	well-mixed	10.9		12		14.0		35.3	
	All	24.6		51		69.5		90.6	
FIRE	upd	10.9		87		36.2		37.4	
[t=21h]	sub	0.8		65		6.6		1.12	
	cld-top	11.5		85		82.7		39.4	
	well-mixed	4.3		219		3.5		2.3	
	All	27.0		456		104		77.6	
			sb		sb		sb		sb
BOMEX	upd	5.8	11.2	57	43	97.5	52.8	87.5	58.9
[t=8h]	sub	1.4	0.3	57	12	15.9	0.50	11.6	0.55
	cld-top	0.47	–	10	–	1.6	–	1.2	–
	well-mixed	4.0	10.9	19	19	5.6	28.5	9.1	19.6
	All	11.5	22.4	143	74	87.7	72.1	85.5	77.9

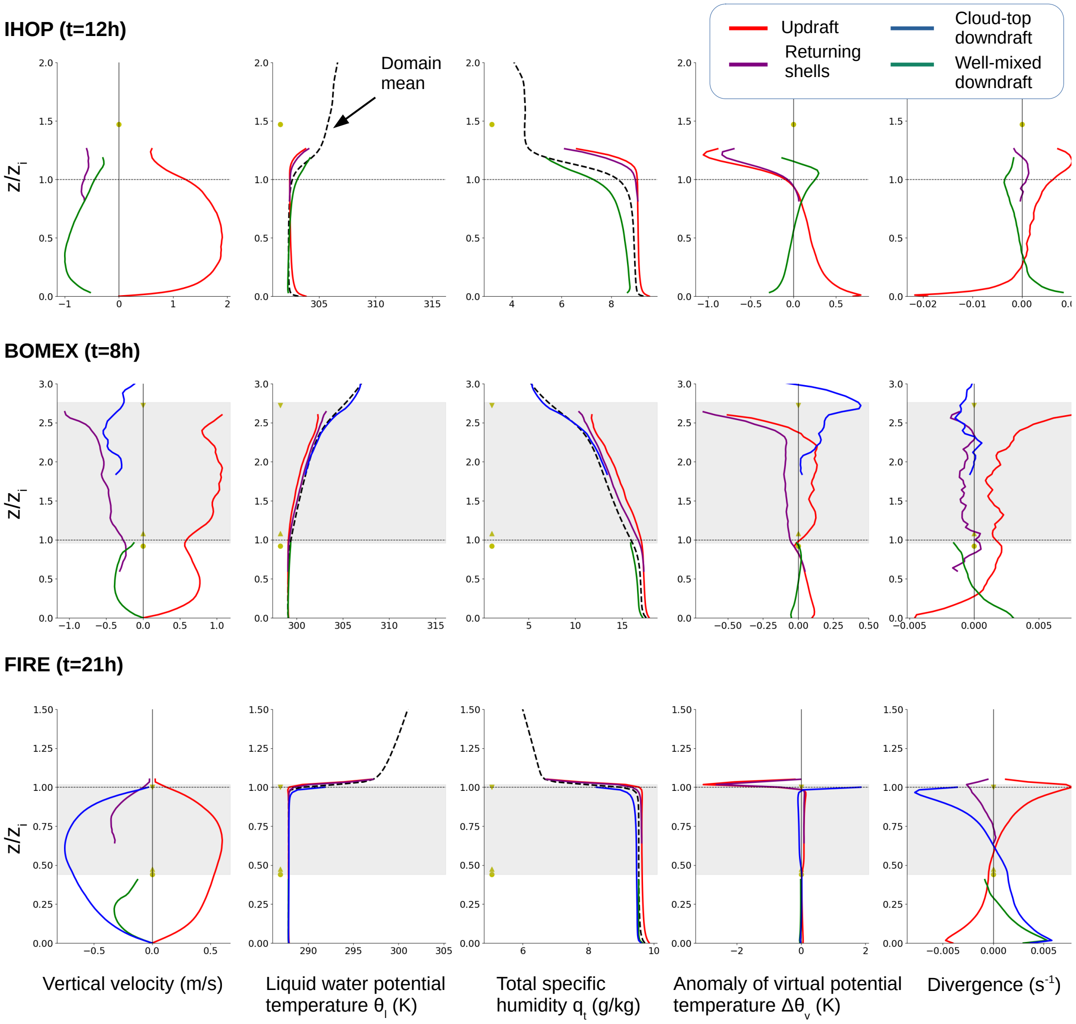

FIGURE 4 Domain-averaged vertical profiles of vertical velocity, liquid water potential temperature, total humidity, virtual potential temperature anomaly, and divergence for IHOP (t=12h), BOMEX (t=8h) and FIRE (t=21h). The dashed black line corresponds to domain mean, and the color lines correspond to object-mean characteristics (updraft, subsiding shell, cloud-top and well-mixed downdrafts are represent as red, purple, blue and green lines respectively). Symbols and horizontal lines are defined in Figure 3. Altitude are scaled by z_i. Object characteristics are only plot if the horizontal-mean object area fraction is higher than 0.5%. Objects are sampled using $V_{\min}$=0.02 km^3 and m=1.

3.2.2 | The marine cumulus boundary layer

Characteristics of the marine cumulus BL differ below and above the cloud base (z=0.6 km~ z_i ; Table 2). Below this level, object features are very similar to those of the dry convective boundary layer (Figure 3 and 4): relative coverage (~20%), bottom-heavy vertical velocity profiles, dry downdrafts and moist updrafts, buoyancy anomalies, and convergence-divergence vertical symmetry. As for the dry BL, object divergence is null where vertical velocity maximizes in the sub-cloud layer. However, updrafts only weakly overshoot above z_i (no significant negative buoyancy). The cross section shows that well-mixed downdrafts seem relatively closed to updraft plumes (Figure 3).

In the cloud layer (0.6-1.7 km), the domain-mean object coverage is reduced (around 5 %) and almost evenly separated between updrafts and subsiding shells (Figure 3). Most sub-cloud upward plumes are thus not strong enough to penetrate the stable layer around z_i. Strong-enough plumes undergo additional acceleration around cloud base due to buoyancy supply by condensation heating (profile of $\Delta\theta_v$ in Figure 4). Being warmer and drier than updrafts, subsiding shells are negatively buoyant, extend downward, and may penetrate the sub-cloud layer. Finally, cloud-top downdrafts occupy a maximum 10% of the domain volume, and brings free-tropospheric dry and warm air downward, only in the upper part of the cloud layer.

3.2.3 | The stratocumulus-topped boundary layer

Contrary to the cumulus BL, the stratocumulus-top BL condensate within the well-mixed layer. The cloud layer extends from the LCL to the inversion layer, with increasing domain-averaged in-cloud water content with height (Figure 3). Locally, updrafts are associated with positive anomalies in liquid water content. By entraining dry, warm free tropospheric air in the well-mixed layer, downdrafts are associated with weaker-than-averaged liquid water content. Conversely, subsiding shells located atop the cloud layer and at the edges of updraft structures have high liquid water content. Sub-cloud downdrafts are located between updrafts and cloud-top downdrafts, and mostly never overlap this latter.

As before, the nighttime stratocumulus BL share similarities with the dry convective BL (Figure 4): object coverage, opposite updraft/downdraft profiles of vertical velocity and divergence, overshooting just above z_i, humidity anomalies of structures, similarities between subsiding shells and updrafts. However, downdraft characteristics have stronger relative amplitudes, which often compare with updrafts'. It is interesting to mention that updrafts end tens of meters higher than where downdrafts start, which suggest weak overshooting by thermal plumes. Condensation heating slightly increases updraft buoyancy that accelerate rising air parcels. Conversely, downdraft buoyancy and temperature (not shown) becomes negative in the cloud layer, probably linked to cloud cooling effects. This negative density anomaly accelerates velocity of subsiding air parcels. Similarities with dry well-mixed layers would suggest that diabatic effects are not the main driver of structures in the nighttime stratocumulus-topped BL. At daytime, object features are slightly different with bi-modal vertical profiles separated at the cloud base (Appendix B).

3.3 | Relative contribution to domain-mean resolved fluxes

The relative contributions of updrafts and downdrafts to the resolved parts of vertical turbulent transport of heat ($\overline{w'\theta_l'}$) and moisture ($\overline{w'q_t'}$) are now investigated. The object flux decomposition and the vertically-averaged object relative contribution follow *Brient et al.* (2019) and are described in appendix C.

In the convective clear-sky BL, updrafts cover only 12.6% of the boundary-layer volume (Table 3) but carry most of heat and moisture (70.8% and 62.6% respectively). Updraft heat transport maximizes at the surface and decreases almost linearly with the altitude, until becoming negative between 0.8 km and 1.2 km which therefore defines the entrainment zone (Figure 5). At this level, subsiding shells slightly compensate this transport. Below the inversion, well-mixed downdrafts cover 10.9% of the BL and contribute to around 14% and 35.3% of the domain-mean resolved heat and moisture fluxes respectively. Carrying less moisture than updrafts, downdrafts nevertheless compete them in the middle of the boundary layer ($0.5z_i$). Overall, objects carry 70-90% of heat and moisture while covering 24% of the

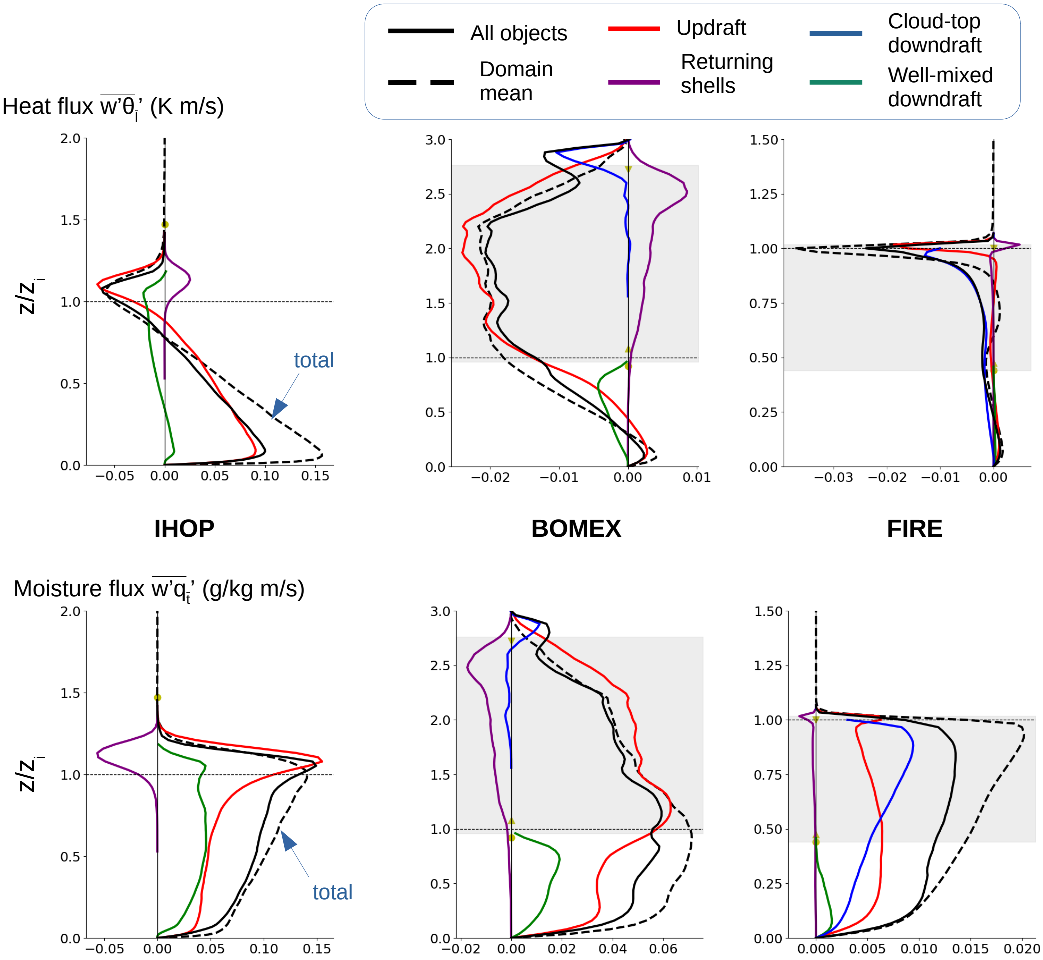

FIGURE 5 Domain-averaged vertical profiles of liquid water potential temperature and total humidity resolved fluxes. Color profiles correspond to mean object characteristics (Table 1). Object contributions to fluxes are weighted by their relative coverage. Domain-mean resolved fluxes are shown as dashed black lines.

volume. The remaining heat transport carried by small-scale eddies is mainly located within the lowest 300m.

In the cumulus BL, condensed plumes contribute to most of heat and moisture fluxes (Figure 5). Transport by subsiding shells cloud-top downdrafts are only significant around the cloud top. Below the cloud base, the flux partitioning shares similarities with the dry BL. Objects represent around 72.1% and 77.9% of resolved heat and moisture transport while covering only 22.4% of the sub-cloud volume (Table 3). Heat is mostly carried by updrafts (52.8%) and well-mixed downdrafts (28.5%). Contrary to the dry BL, moisture is carried three times more by updrafts (58.9%) than by well-mixed downdrafts (19.6%).

For the stratocumulus-topped boundary layer, the flux partitioning has already been extensively described in *Brient et al.* (2019). Here, we confirm the relative importance of downdrafts in moisture transport (Figure 5 and table 3), and show that new objects (sub-cloud downdrafts and subsiding shells) are less important. Covering 27% of the domain volume average, coherent structures contribute to around 77.6% of resolved moisture fluxes. The missing part is mostly located in the 200m below the cloud top. Note that the domain-mean total heat vertical flux profile is weak, except just below the cloud top. Daytime object contribution to fluxes are described in appendix B.

Performing a similar analysis at different time steps confirms these conclusions (Appendix D), yet with a diurnal evolution of stratocumulus (*Brient et al.*, 2019). This invariance in time suggests that (1) analyzing one snapshot is relevant for studying the BL dynamics, (2) the relative contribution of objects signs the type of boundary layer (continental vs marine, cloudy or not), and (3) the relative object contribution to turbulent fluxes in a given mixed layer is not influenced by a deepening of the mixed layer.

Our analysis highlights that downdrafts identified in well-mixed layers carry a non-negligible part of heat and moisture (between 20 and 40%). Defined by tracers emitted above these layers, they always entrain warm and dry air in the boundary layer. Despite that air parcels start positively buoyant (Figure 4), convergence might help them to sink vertically until they reach the surface. The fact that downdrafts are initiated against local environmental density and that condensation is not a mandatory process suggests that downdraft triggering is forced (mechanistic-driven) and thus not driven by diabatic effects, such as evaporating and radiative cooling. In that context, an extra source of cooling, such as cloud radiative cooling in the stratocumulus-topped boundary layer, only enhances the strength of dry downdrafts. We now investigate roots of downdrafts by investigating spatial organisations of coherent structures.

4 | INVESTIGATING ROOTS OF DOWNDRAFTS WITH THE MESOSCALE ORGANISATION

4.1 | Dry downdrafts

4.1.1 | Spatial organisation of the dry convective boundary layer

At the inversion layer z_i, the dry convective BL organize as a cellular pattern with cells sizes of 2 km, i.e. around $2z_i$ (Figure 2). Updrafts are located at the center of these cells, with subsiding shells attached to them (Figure 6). Relatively large areas of positive moisture anomalies encompass several updrafts. Conversely, the mesoscale organisation of vertical velocity is smaller and scales with updrafts' sizes. Downdrafts are located close to updrafts, and underline the border between areas of positive/negative relative humidity anomalies. Slightly below the inversion (not shown), downdrafts organize as elongated structures of strong negative moisture anomalies and vertical velocity. Close to the surface (z=0.25 z_i – Figure 6), updrafts are small, roughly circular, and organize as thin bands. Downdrafts are located between these elongated lines of updrafts organized in circles, as clearly seen on the vertical velocity field. As suggested in Figure 4, the mesoscale pattern of convection close to the surface seems to confirm a link between updrafts' convergence and downdrafts' divergence close to the surface.

In order to better understand the initiation of downdrafts, we focus on a subdomain around the inversion (Figure 7). It shows that downdrafts initiate within the entrainment zone [$0.9z_i$-$1.1z_i$] in the vicinity of each updraft. As they sink, downdrafts grow and eventually merge. This merging mechanism is associated with negative humidity anomalies, and positive θ_v anomalies (not shown). Therefore, dry downdrafts are likely related to mass convergence induced by updrafts (and likely the relative proximity between each other). This is likely different of updrafts' triggering that is related to air parcels having positive buoyancy that rise them, despite obvious near-surface convergence. This suggest that downdrafts are part of an overturning circulation within a well-mixed boundary layer.

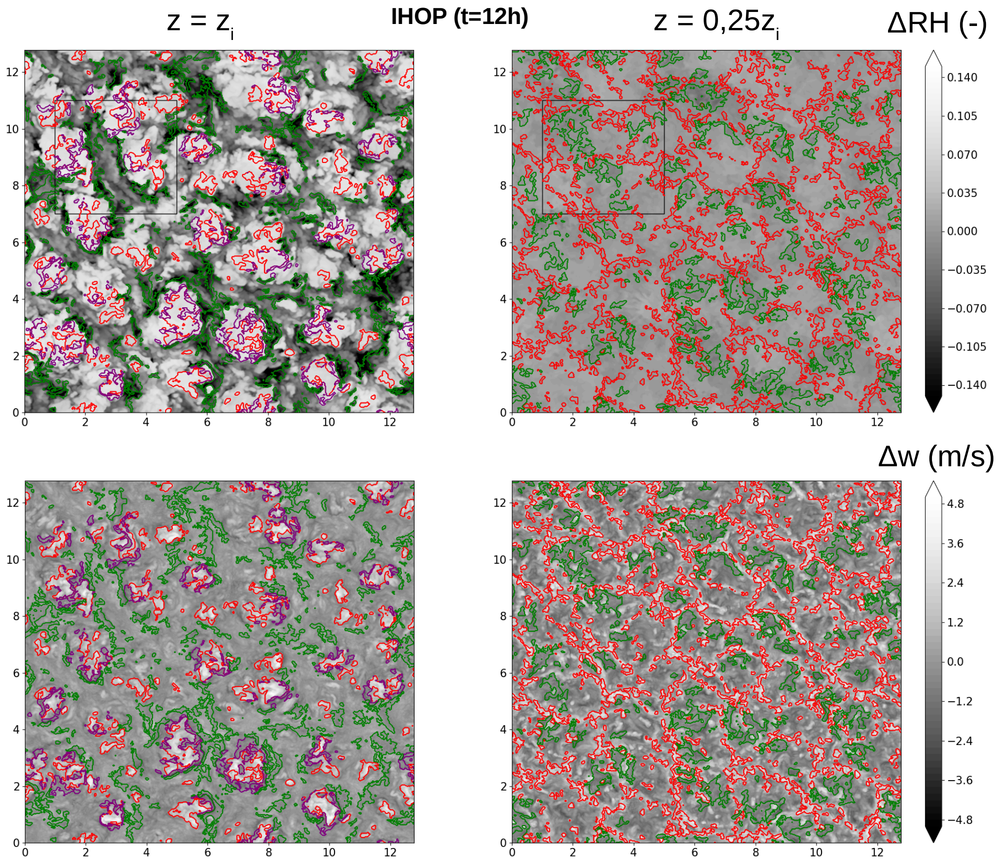

FIGURE 6 Anomalies of relative humidity (top) and vertical velocity (bottom) relative to the domain average at the inversion z_i (left) and 0.25 z_i (right) for IHOP (t=12h). Object-defined updraft plumes, subsiding shells and dry tongues are represented as red, purple and green contours respectively. Black squares are the subdomain shown on Figure 7.

4.1.2 | Mesoscale organisation of cumulus (without horizontal winds)

In order to simplify the interpretation of the sub-cloud mesoscale organisation, we perform a modified BOMEX simulation with no large-scale horizontal winds (setting horizontal wind forcing to zero). The domain-mean characteristics and object relative contributions are very similar, which confirm our ability to use this simulation to study sub-cloud downdrafts (not shown).

Without large-scale winds, clouds are small, numerous, and show no sign of specific spatial organisation (Figure 8). Each updraft is roughly separated by a distance of around 1 km (1.7 z_i). A focus on a subdomain confirms that the sub-cloud layer share similarities with the dry convective boundary layer. Around z_i, updrafts trigger horizontal divergence of moist air parcels. Downdrafts are located over regions of low humidity and are associated with air convergence. At the surface, an interconnected network of updrafts' lines is even more striking than over the dry boundary layer. Downdrafts end at the center of cells defined by different updrafts' lines, which confirm that downdrafts constrain

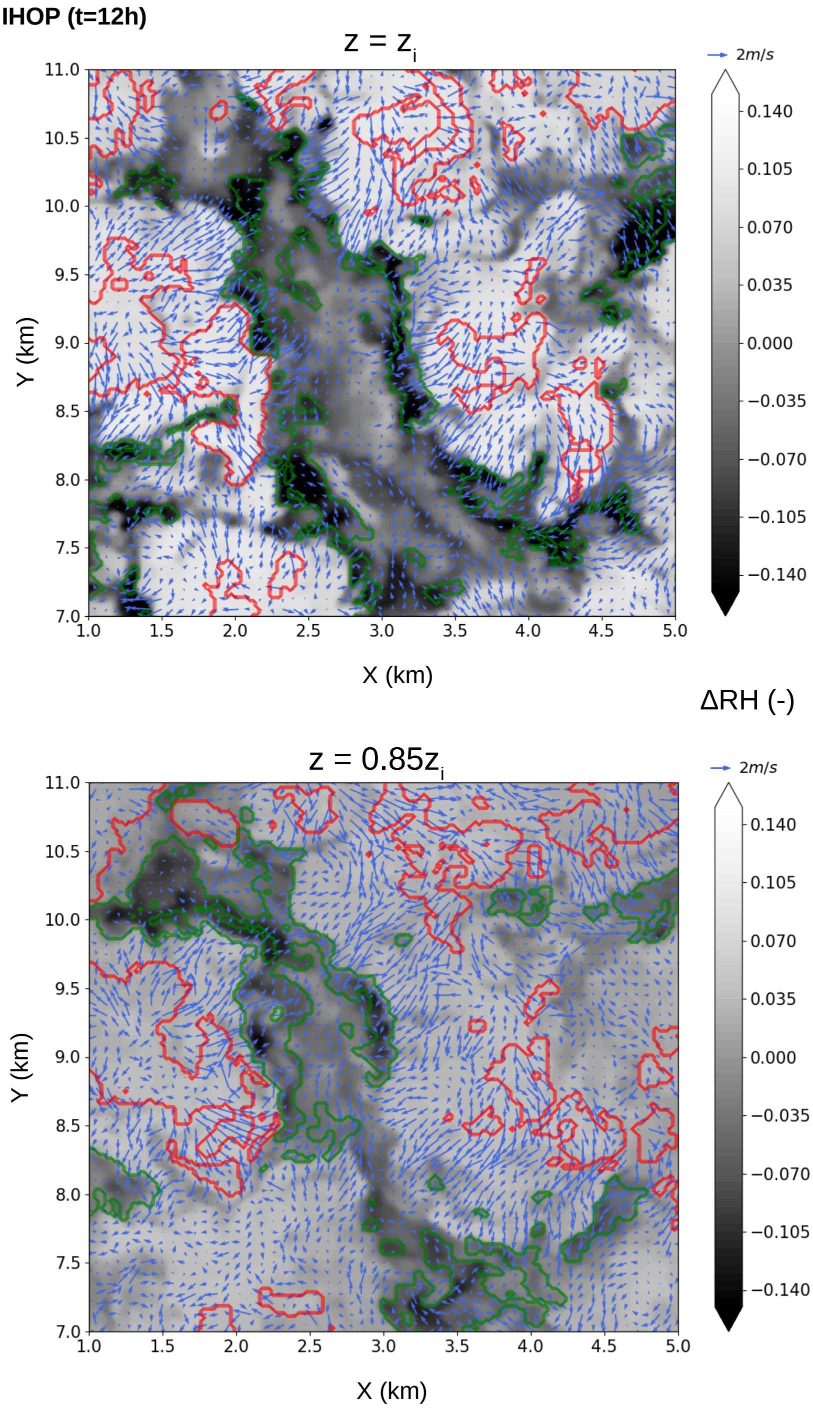

FIGURE 7 Anomalies of relative humidity at z_i and 0.85 z_i for IHOP (t=12h) over the subdomain shown in Figure 6. Object-defined structures are similar as in figure 6, without subsiding shells for clarity. Anomalies of horizontal wind speed are overlapped as blue arrows.

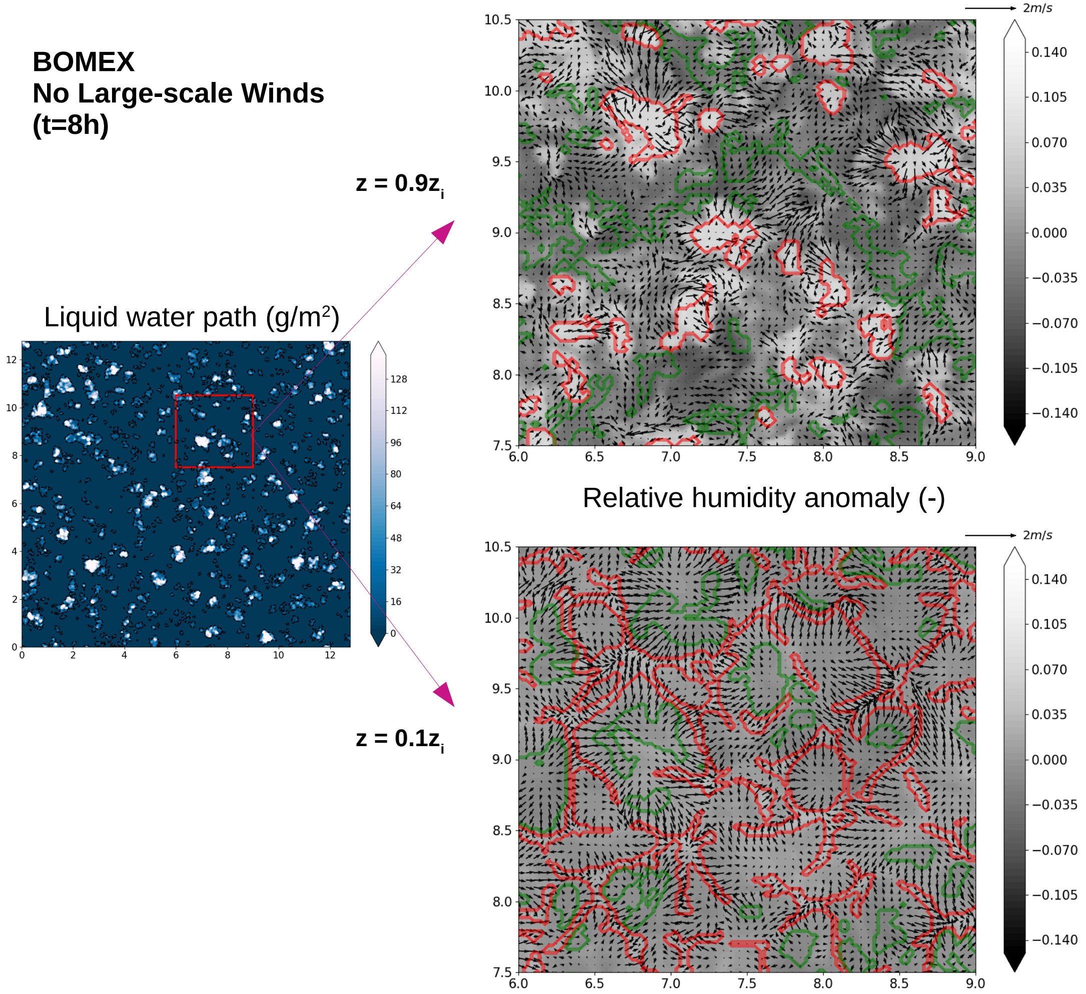

FIGURE 8 Liquid water path over the full domain of the BOMEX simulation without large-scale winds at t=8h. The right panel shows anomalies of relative humidity relative to the domain average zoomed over a subdomain, both around the inversion (0.9 z_i) and at z=0.1 z_i. Object-defined updraft plumes, subsiding shells and dry tongues are defined in Table 3. Anomalies of horizontal winds are shown as black arrows.

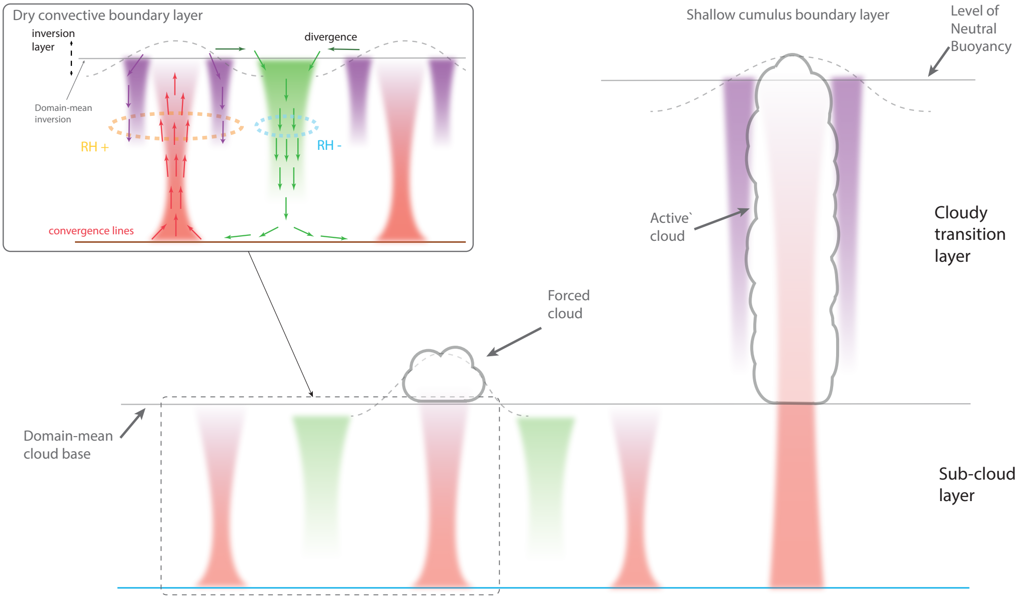

FIGURE 9 Schematic of coherent structures in the clear-sky and cumulus convective boundary layer. Updrafts, subsiding shells and downdrafts are represented in red, purple and green respectively. Domain-mean inversion layer, cloud base, and level of neutral buoyancy are represented as a straight grey lines and local perturbation as dashed grey lines. For the dry convective boundary layer (top-left panel), positive and negative anomalies of relative humidity are represented in orange and blue respectively. In the first tens of meters, origin of updrafts are horizontal convergence lines. The sub-cloud layer share similarities with the continental dry convective boundary layer.

the narrow lines of convergence and thus have a active role in shaping the spatial BL organisation. The absence of large-scale wind forcing allows us to better show the vertical sinking of subsiding coherent structures from the inversion to the surface, but also the updraft growth from hubs of convergence lines. Such spoke-like pattern, already been highlighted by *Schmidt and Schumann* (1989) and *Williams and Hacker* (1993), shows cell sizes that roughly equal the depth of the well-mixed layer (z_i=600 m).

Similarities between the sub-cloud layer and the dry convective BL suggest a negligible role of clouds for triggering coherent downdrafts and organized the well-mixed convective layers. However, clouds may influence the transition layer and thus the local mixing at the inversion (*Albright et al.*, 2023).

4.1.3 | Conceptual view

Analysis of thermodynamical characteristics and spatial organisation allows us to provide a sketch of coherent structures in clear-sky convective boundary layers (Figure 9).

At the surface, updrafts organize in horizontal convergence lines that gather at locations where air parcels start having positive vertical velocity and buoyancy. Around the inversion where the boundary layer is less mixed, updrafts slow down, overshoot stable layers and start becoming negatively buoyant over a relatively thin layer. This induces subsiding returning shells located around updraft structures.

Each downdraft starts at boundaries of a dome previously formed by one updraft, moves away by updraftgenerated divergence, and eventually sinks. Between several updrafts, downdrafts gather together and create a coherent subsiding structure that extent downward in the well mixed boundary layer (dry tongue). Started with positively-buoyant air parcels, downdrafts are adiabatically triggered by convergence of air masses, and entrain dry air parcels that originate from the free troposphere. This suggests that downdrafts are constrained by the boundary-layer dynamics, and probably influenced by the relative proximity of updraft plumes. Not to be confused with driving mechanisms of subsiding shells, downdrafts can be considered as the compensating coherent subsidence of updrafts.

In the sub-cloud layer of cumulus regime, well-mixed downdrafts are also triggered by divergence of air masses and entrain dry, warm air. For forced clouds that do not become positively buoyant by condensation heating, the sub-cloud overturning circulation remains similar. For active clouds, subsiding shells around updrafts reach the sub-cloud layer but does not seem to significantly influence it. However, these clouds generate gravity waves that homogenize temperature in the cloud layer, and indirectly influence entrainment rate. Finally, large-scale horizontal winds perturb this equilibrium by helping gathering together small updrafts into larger ones, but does not refute the schematic view of Figure 9.

4.2 | Stratocumulus-topped downdrafts

4.2.1 | Spatial organisation

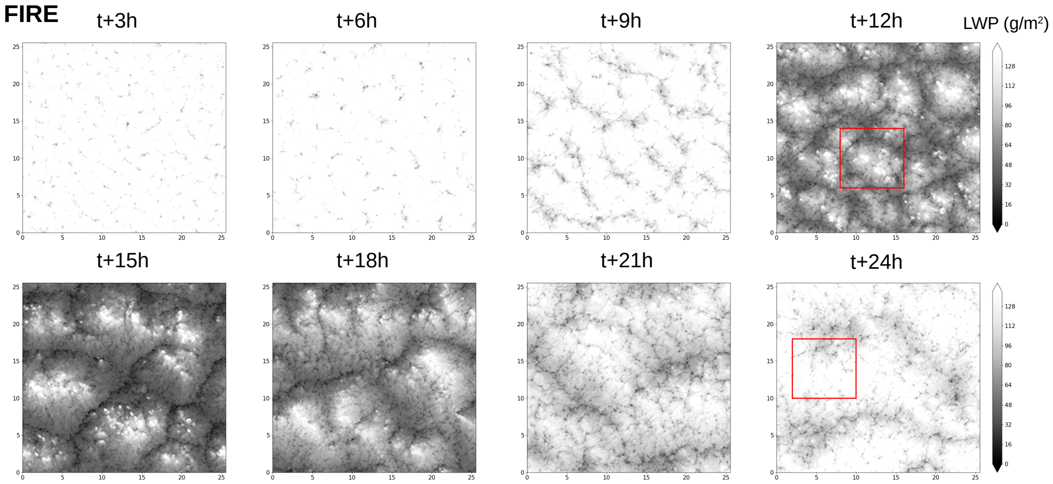

FIGURE 10 Liquid water path (g/m^2) for the FIRE simulation between t=3h and t=24h. Red squares represent subdomain areas highlighted in Figure 11

Contrary to previous BL, the spatial organisation of the stratocumulus-topped boundary layer significantly vary in time, with the lowest liquid water content at daytime and the largest at nighttime (Figure 10). At daytime, a cellular pattern is visible with cell sizes of around 5 km at 12:00 and 8-10 km at 15:00. Note that local positive anomalies exist within cells. With sunset, liquid water path increases and the mesoscale cellular organisation start vanishing.

Zooming over subdomains close to the inversion highlights relationship between updrafts and downdrafts (Figure 11). At daytime, updraft structures are associated with divergence of air masses, and downdrafts start where convergence prevails. Downdrafts organize in thin lines and are significantly associated with low liquid water content.

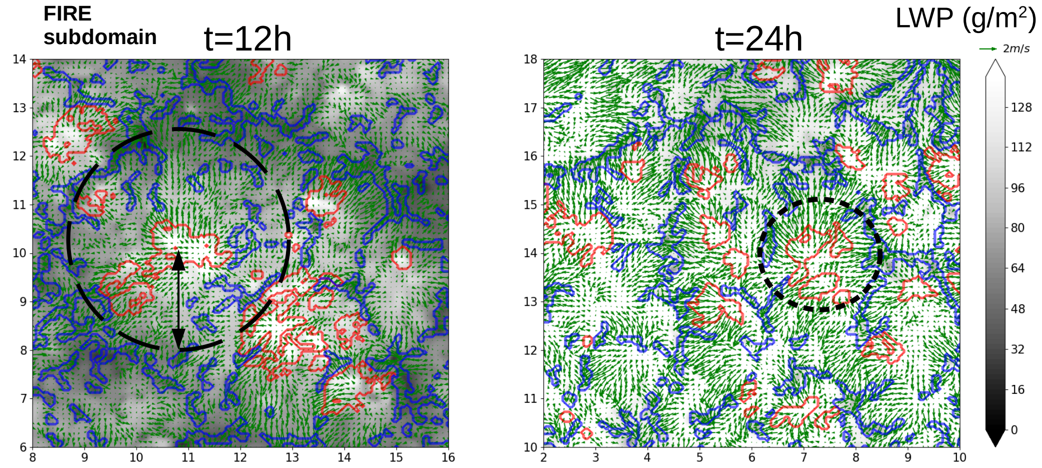

FIGURE 11 Liquid water path (g/m^2) over FIRE subdomains shown in Figure 10 at t=12h and t=24h. Updrafts and downdrafts are represented in red and blue contours respectively, and horizontal winds as green arrows for the altitude z=0.95z_i. Black circles show regions influenced by one updraft's divergence.

At nighttime, updrafts are more numerous and less distant to each other. Downdrafts are also more numerous and located in regions of air convergence. The area influenced by one updraft's divergence changes in time, with larger areas at daytime (circle in Figure 11). The relative proximity of updrafts might thus influence how downdrafts organize.

While the nighttime BL shares characteristics with the dry convective BL (section 3.2.3), it is different at daytime (Appendix B). Figure 12 shows that the daytime reduction in objects' volumes is related to the stronger difficulty updrafts have to deepen to the BL top, as shown by the averaged maximum altitude ascending structures can reach (Figure 12b). This lower updraft altitude is associated with the smallest number of updrafts reaching the BL top (as shown in Figure 11). While nighttime downdrafts reach the surface, daytime objects are vertically shorter and less likely to reach the surface (Figure 12d). Since downdrafts shape surface divergence, updrafts' locations and triggering, their diurnal modification likely influences the BL spatial organisation of convective structures and thus the visible mesocale organisation (Figure 10).

4.2.2 | Mass flux and decoupling

The diurnal vertical extension of structures is also associated with the temporal evolution of the objects' mass flux M_i (kg/m^2/s) defined as:

$$M_i = \frac{1}{z_i}\int_0^{z_i} \Omega_i(z)\cdot dz \qquad (4)$$

$$\text{with } \Omega_i(z) = \sum_{(x,y)\in i} \overline{\alpha_i}(z)\overline{\rho}(z)\left(w(x,y,z)-\overline{w}(z)\right) \qquad (5)$$

with $\overline{\alpha_i}$ (%) the relative fraction of object type i and ρ the air density. Figure 12c shows that solar warming reduces both updrafts' and downdrafts' fluxes. Note that updrafts and downdrafts mostly cancel each other, which give a roughly constant negative total mass flux carried by objects. This suggests compensating ascendance at the domain

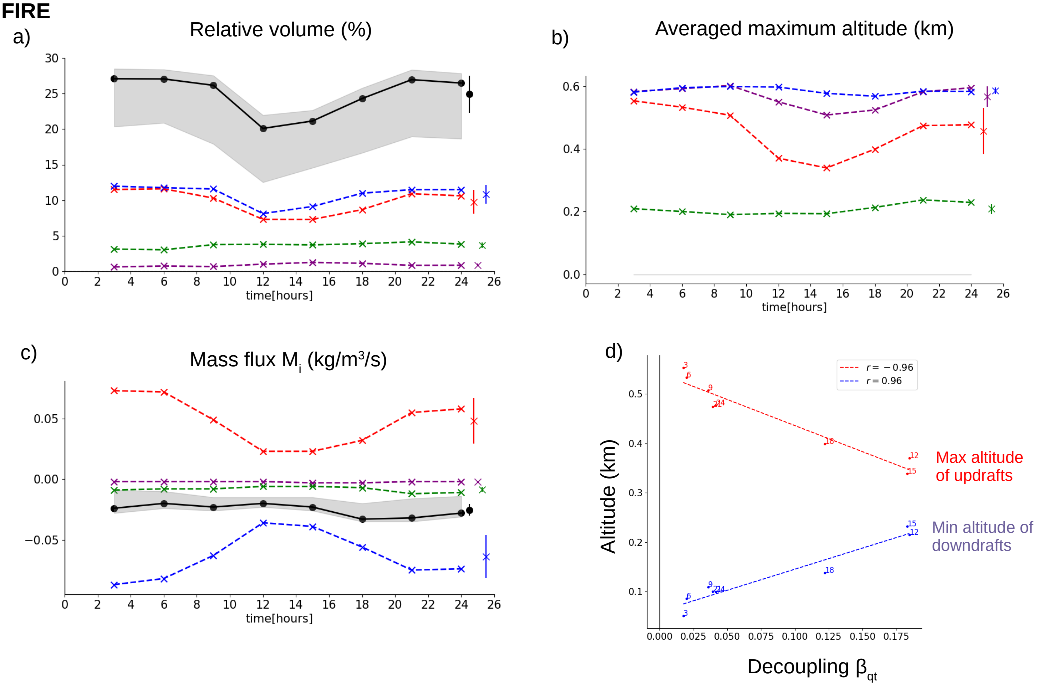

FIGURE 12 Time evolution of (a) vertically-averaged relative object volume, (b) maximum averaged altitude reached by objects, and (c) vertically-averaged mass flux for the FIRE simulation. Updraft, subsiding shells, sub-cloud downdraft and cloud-top downdrafts are represented as red, purple, green, and blue lines. Charactertistics summed over all objects are represented with a black line for V_{min}=0.02 km^3, with the shaded grey area showing sensitivity of V_{min} ranged between 0.005 and 0.5 km^3. (d) Relationship between the decoupling index β_{q_t} and both object-averaged updraft maximum altitudes (red) and downdraft minimum altitudes (blue). Numbers represent time of the simulation and correlation coefficient of slope are added at the top-right side.

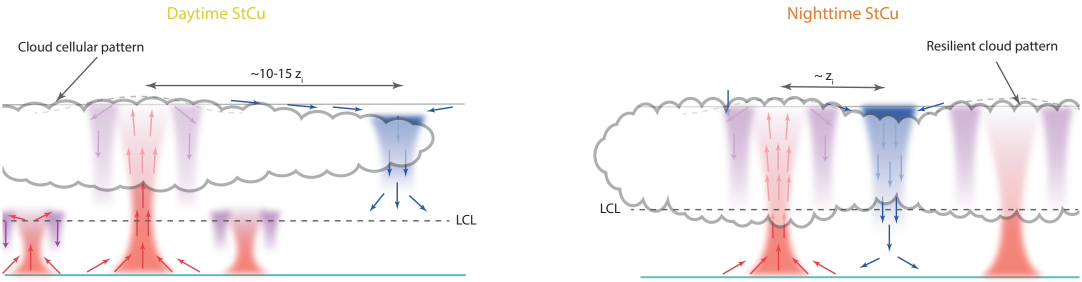

FIGURE 13 Schematic of coherent structures in the stratocumulus-topped boundary layers (StCu) at daytime (left) and nighttime (right). Updrafts, subsiding shells and cloud-top downdrafts are represented in red, purple and blue respectively. Domain-mean inversion layer z_i and lifting condensation level (LCL) are represented as rigid and dashed grey lines respectively. Local perturbation of z_i are shown as dashed grey lines. At daytime, the cloud layer thins and a mesoscale cellular pattern is visible. At nighttime, the overturning circulation of coherent structures is roughly similar to the dry boundary layer and is embedded in a resilient mesoscale cloud organisation. Sub-cloud downdrafts are not shown in the schematic.

size.

Solar irradiance warms the cloud layer, which perturb vertical gradients of temperature. This results in a less efficient coupling of clouds with the surface moisture supply, which thus increases sub-cloud humidity. The decoupling strength can be quantified through different indexes, such as the convenient way used in *De Roode et al.* (2016):

$$\beta\phi = \frac{\phi_{cld} - \phi_{ML}}{\phi_{z+} - \phi_{ML}} \tag{6}$$

with ϕ a variable such as q_t or θ_l. Subscripts cld and ML represent values averaged between the domain-mean cloud base and cloud top, and between the surface and cloud base respectively. ϕ_{z+} corresponds to the domain-mean value one layer above z_i. The decoupling parameter β_ϕ is close to zero if the boundary layer is well mixed, i.e. ϕ is similar above and below the cloud base. Figure 12d shows strong correlation between β_{q_t} and updrafts' (maximum) and downdrafts' (minimum) altitudes. High correlations are also shown for β_{θ_l} ($|r|$>0.95 – not shown). Therefore, BL decoupling induced by cloud warming and drying significantly influences the vertical development of structures and their mass flux.

4.2.3 | Conceptual view

Figure 13 shows a sketch of coherent structures in daytime and nighttime stratocumulus-topped boundary layers.

At daytime, solar warming induces a weak stable layer close to the domain-mean cloud base. This induces convection inhibition that modifies the organisation of updrafts, which need to gather to penetrate this stable layer, and thus influences how downdrafts are triggered and develop. Boundary-layer decoupling reduces the number and volume of coherent structures, their vetical devlopment, and the updrafts' and downdrafts' mass fluxes. This induces an observable cellular cloud pattern with cell sizes of around 5-10 km (i.e. 10-15z_i), which is thus a strong signature of the daytime decoupling. This is in agreement with *Zhou and Bretherton* (2019a).

At sunset, the nighttime boundary layer becomes well mixed again and shares similarities with the dry convective boundary layer (Figure 9). The reduction of decoupling increases objects' volume, vertical extension and mass

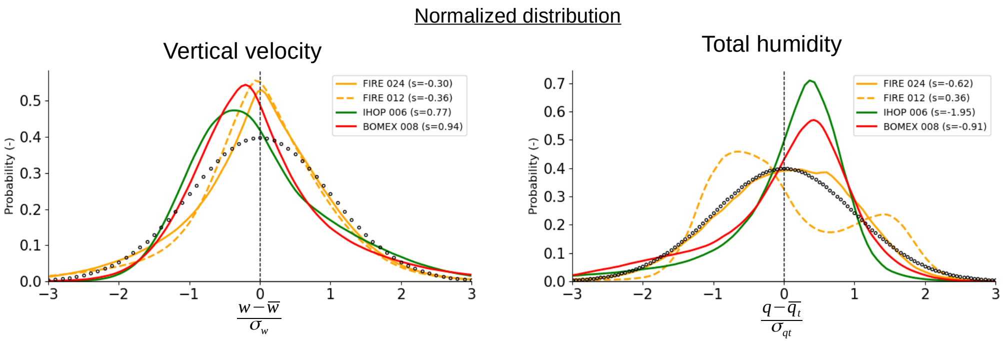

FIGURE 14 Probability density function of normalized vertical velocity (a) and total humidity (b) of all points between the surface and the well-mixed boundary layers z_i for IHOP (t=12h), BOMEX (t=8h), and FIRE (t=24h). Variables are normalized by the standard deviation σ and mean μ of the distributions. The standard normal distribution is represented as black circles.

flux almost to values before sunrise. However, a mesoscale cloud pattern remains, which is more a signature of the resilience of the diurnal disturbance than a true nocturnal structural organisation (Figure13).

5 | CONCLUSIONS

In the present work, we analyze subsiding structures in high-resolution simulations of three boundary layers: continental clear sky convection, marine cumulus, and stratocumulus topped boundary layers. A object-oriented methodology is used to identify tri-dimensional coherent structures based on passive tracers emitted at different levels: surface, just above cloud top, and above the well-mixed layer (or cloud base if available). Additionally, a conditional sampling based on vertical velocity separates ascending and subsiding structures. This leads to identify four different coherent structures: updraft, subsiding shells, cloud-top downdrafts, and well-mixed downdrafts.

Similarities exist across well-mixed parts of boundary layers. Warm and moist updrafts cover the largest part of the domain (10-12%), are related to surface convergence of air parcels, accelerate until the middle of the mixed layer, and show divergence at the top of the boundary layer. Surrounding updrafts, subsiding shells have similar thermodynamical characteristics than them. Defined through entrained warm and dry air parcels from the free troposphere, well-mixed downdrafts are related to air mass convergence atop the boundary layer and accelerate downward until potentially reaching the surface. Well-mixed downdrafts start positively buoyant which suggests that subsidence starts against gravity.

Updraft structures carry most of heat and moisture within the well-mixed layers, with different relative amplitudes for the clear-sky convective boundary layer (62-70% of the total resolved flux), the sub-cloud layer of the cumulus regime (52-58%), and the stratocumulus layer (36-37%). Conversely, subsiding shells carry less heat and moisture (0.5-7%). In all boundary layers, well-mixed downdrafts carry a significant part of heat and moisture, especially in stratocumulus layer (39%) but also in dry layers such as the continental clear sky layer (14-35%) and the sub-cloud layer of the cumulus regime (19-28%). This confirms previous work that have showed the relative importance of downdrafts in stratocumulus layers (*Davini et al.*, 2017; *Chinita et al.*, 2018; *Brient et al.*, 2019) and in the dry convective boundary layer (*Couvreux et al.*, 2005).

The importance of subsiding coherent structures in carrying heat and moisture imposes a robust understanding of processes explaining them. Figure 9 highlights an overturning circulation of horizontal length scale of around the boundary-layer depth (i.e. aspect ratio of 1-2), which involve bottom-up and top-down coherent structures that influence each other. At the surface, downdrafts' divergence force lines of convergence that fueled updrafts' rising of warmer, positively buoyant air parcels. At the boundary-layer top, similar mechanisms occur with updrafts' divergence generating downdrafts' convergence lines. However, the smooth boundary that allow entrainment of air in the mixed layer distort this canonical view. This mesoscale circulation shares strong similarities with the Rayleigh-Bénard convection instability driven by a density-stratified fluid confined between two isothermal no-slip boundaries (*Willis and Deardorff*, 1979; *Couston et al.*, 2017). It is partly confirmed by the gaussianity of the normalized distributions of vertical velocity w and total humidity q_t for the nighttime stratocumulus layer (Figure 14), as one should expect from the canonical Rayleigh-Bénard theory.

For the dry boundary layers (IHOP and BOMEX), distributions are skewed, positively for vertical velocity and negatively for humidity. It suggests that faster updrafts than downdrafts, but the dry anomalies carried by downdrafts are more extreme. These skewnesses might be related to the weakest stability between the mixed layer and the free troposphere in IHOP and BOMEX, which increases the entrainment rate and thus deforms the canonical Rayleigh-Bénard convection (*Couston et al.*, 2017).

Finally, the humidity distribution of the stratocumulus layer shows a bimodal, positively skewed distribution, which implies that updrafts transport stronger positive moisture anomalies than during nighttime. Conversely, the strongest downdrafts carry less dry parcels than during daytime. While mechanisms remain to be better understood, this bimodal distribution is very likely associated with the boundary-layer decoupling and the cellular mesocale pattern highlighted only when solar irradiance warms the boundary layer (Figure 10).

This analysis challenges the actual concept of representing coherent boundary-layer structures in climate models. Most climate models use mass-flux assumptions for representing rising coherent structures, associated with eddy diffusivity assumptions and compensating subsidence at the sub-grid scale. Here we suggest that coherent downdrafts should also be represented, yet following some conditions. First, downdrafts are part of an overturning circulation and thus connected with updrafts. Lateral entrainment and mass conservation are thus necessary. Second, downdrafts' triggering should be thought adiabatically (since they exist in dry boundary layers) and be allowed to carry dry, warm air from above the boundary layer. Diabatic perturbations (cloud radiative cooling, phase change) and entrainment rate would perturb this triggering. Third, boundary-layer decoupling should be taken into account to modify strength of rising and subsiding transport. Overall, this calls for investigating about how the mesoscale organisation of coherent structures should be taken into account at the sub-grid scale.

In that purpose, ongoing work focuses on modifying the thermal plume model implemented in the LMDZ climate model (*Hourdin et al.*, 2002, 2020) to take into account these coherent subsiding structures. The relative role of new parameterizations of coherent downdrafts to local diffusivity and/or compensating subsidence needs to be quantified for improving simulating atmospheric boundary layers. Further investigations targeting similarities between atmospheric boundary layers and the Rayleigh–Bénard convection might also be an asset to improve boundary-layer parameterizations (*Shipley et al.*, 2022).

TABLE 4 Setup of simulations for the three boundary layers

Case	Domain Size (km^3)	Resolution Dx/Dz (m)	Time step (s)	Reference
IHOP	12.8x12.8x4.0	25/stretch	1	*Couvreux et al.* (2005)
BOMEX	12.8x12.8x4.0	25/25	1	*Siebesma et al.* (2003)
FIRE	25.6x25.6x1.2	50/10	1	*Duynkerke et al.* (2004)

TABLE 5 Surface and large-scale forcings for the three boundary layers. SH and LH are sensible and latent heat fluxes. Brackets show the evolution in time.

Case	Type	Surface T (K)	SH (W/m^2)	LH (W/m^2)	Forcings	Winds
IHOP	Land	[296→304]	[5→304]	[22→176]	Cooling/Drying	Southeasterly
BOMEX	Ocean	298.7	9.2	154	Cooling/Drying	Easterly
FIRE	Ocean	289	Interactive		Cooling/Moistening	Northwesterly

A | CHARACTERISTICS OF SIMULATIONS

The Meso-NH model version 5.4.2 (*Lafore et al.*, 1998; *Lac et al.*, 2018) is used to reproduce three different BL regimes: the IHOP clear-sky convective BL (*Couvreux et al.*, 2005), the BOMEX marine cumulus (*Siebesma et al.*, 2007) and the FIRE stratocumulus (*Duynkerke et al.*, 2004). Table 4 and 5 show domain characteristics and model setup.

Simulations share strong similarities in terms of parameterizations (Table 6). The model uses an anelastic system of equations and a 3D turbulence scheme with a 1.5-order closure, involving prognostic turbulent kinetic energy (TKE) and a diagnostic mixing length (*Deardorff*, 1980). The conservative variables used in prognostic equations are advected with a positive definite fourth-order centered scheme. Temporal scheme for momentum advection uses the Runge-Kutta centered fourth-order scheme. The different water phase transformations are parameterized either with the one-moment mixed ICE3 scheme (*Caniaux et al.*, 1994; *Pinty and Jabouille*, 1998), or with a 2-moment warm microphysics parameterization for stratocumulus layers (*Khairoutdinov and Kogan*, 2000; *Geoffroy et al.*, 2010). Finally, radiative tendencies are either switched off for clear-sky layers, imposed through a prescribed long-wave profile for cumuliform clouds, or computed based on a two-stream method following the ECMWF assumptions (*Lac et al.*, 2018).

TABLE 6 Parameterization schemes

Case	Advection	Temporal	Radiation	Microphysics	Turbulence
IHOP	4^{th} cent.	4^{th} Runge-Kutta	No	No	1.5-order
BOMEX	-	-	Prescribed LW	mixed (ICE3)	-
FIRE	-	-	ECMWF	2-mom. warm (KHKO)	-

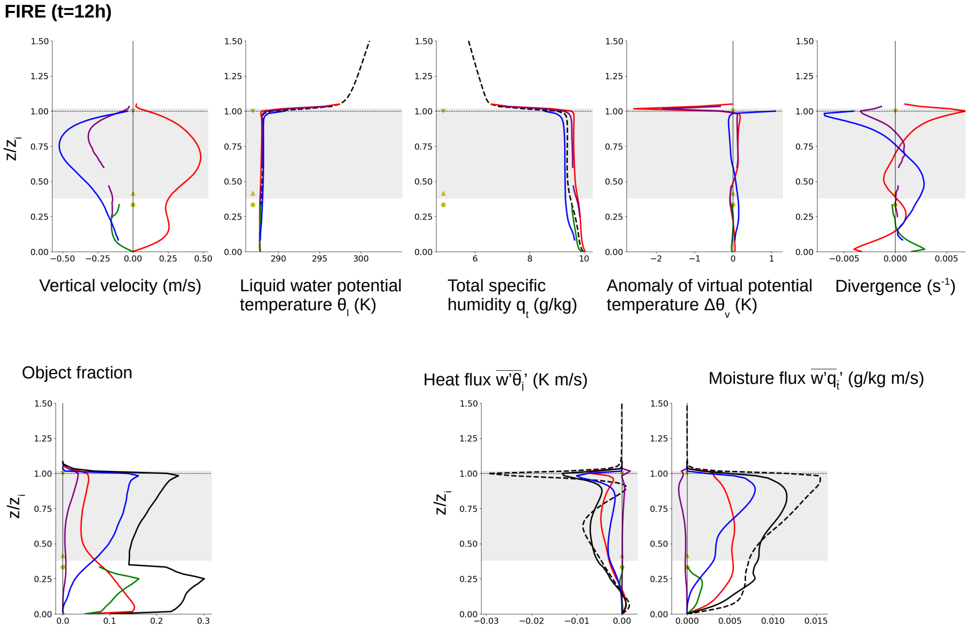

FIGURE 15 Domain-averaged vertical profiles of features described in Figure 3, object relative fraction for FIRE at t=12h. Domain-averaged vertical profiles of liquid water potential temperature and total humidity resolved fluxes. Color profiles are described in Figure 3, Figure 5 and table 1. Object characteristics are only plot if the horizontal-mean object area fraction is higher than 0.5%. The cloud layer is showed as the grey area and objects are sampled using V_{min}=0.02 km^3 and m=1.

B | CHARACTERISTICS OF THE DAYTIME STRATOCUMULUS

At daytime, the relative fraction shows a sharp decrease around the domain-mean cloud base for both updrafts and downdrafts (Figure 15). Subsiding shells are present both at the top of the cloud layer and around the LCL, and sub-cloud downdraft fraction cover around 12%. Around cloud base, updrafts show vertical velocity increase due to latent heat release by condensation, negative buoyancy, and air mass divergence. In the cloud layer, object features are similar as those at nighttime. This suggests two overturning circulations: one that is weakly-developed below cloud base and compensated by sub-cloud downdrafts, and one carried by the strongest updrafts compensated by cloud-top downdrafts. At daytime, updrafts carry slightly more heat and moisture than downdrafts (Figure 15).

The daytime area fraction of coherent structures resemble more the cumulus case than the clear-sky convective layer (oppositely at nighttime).

C | OBJECT CONTRIBUTION TO FLUXES

At altitude z, the vertical transport $\overline{w'\phi'}$ can be decomposed into a sum of different object contributions $F_i(\phi,z)$ defined as

$$\overline{w'\phi'}(z) = \sum_i F_i(\phi, z) \tag{7}$$

$$\text{with } F_i(\phi, z) = \frac{1}{N} \sum_{(x,y)\in i} (w(x,y,z) - \overline{w}(z)) \cdot (\phi(x,y,z) - \overline{\phi}(z)) \tag{8}$$

with i the different conditional sampling or the environment (i.e., no CS), ϕ a conservative variable (θ_l or q_t), and N the number of horizontal cells. Bar and prime represent the horizontal mean and the anomaly relative to this average respectively. F_i quantifies the relative contribution of each component to the boundary-layer turbulent transport and is the sum of the top-hat contribution to fluxes and the covariance within structures (*Siebesma and Cuijpers*, 1995; *Wang and Stevens*, 2000; *Chinita et al.*, 2018). Following *Brient et al.* (2019), the vertically-averaged object relative contribution to domain-averaged resolved fluxes $< F_i(\phi) >$ is defined as:

$$< F_i(\phi) > = \frac{\int_z |F_i(\phi, z)|}{\int_z |\overline{w'\phi'}(z)|} \tag{9}$$

This formulation aims to quantify vertical transport independently to its sign. The vertical transport for the three considered boundary layers is shown in Figure 5, and their vertical averages are listed in Table 3.

D | TEMPORAL EVOLUTION OF OBJECT CHARACTERISTICS

As boundary layers change in time (Figure 1), the evolving boundary-layer dynamics may ultimately influence the relative object contribution to resolved fluxes. To verify to what extent results are sensitive to boundary-layer changes, we characterize flux contributions at different time step.

Figure 16 shows the temporal evolution of object contributions to turbulent fluxes averaged over well-mixed layers (below the cloud base for the cumulus regime). While the boundary layer evolves in time, their relative contributions remain constant. It is shown for both total and individual contributions, yet with the exception for the StCu layer where object contributions of heat transport are influenced by the daytime shortwave warming and cloud thinning (Appendix B and section 4.2). Conversely, the IHOP diurnal clear-sky BL deepening does not modify the relative contribution of object fluxes.

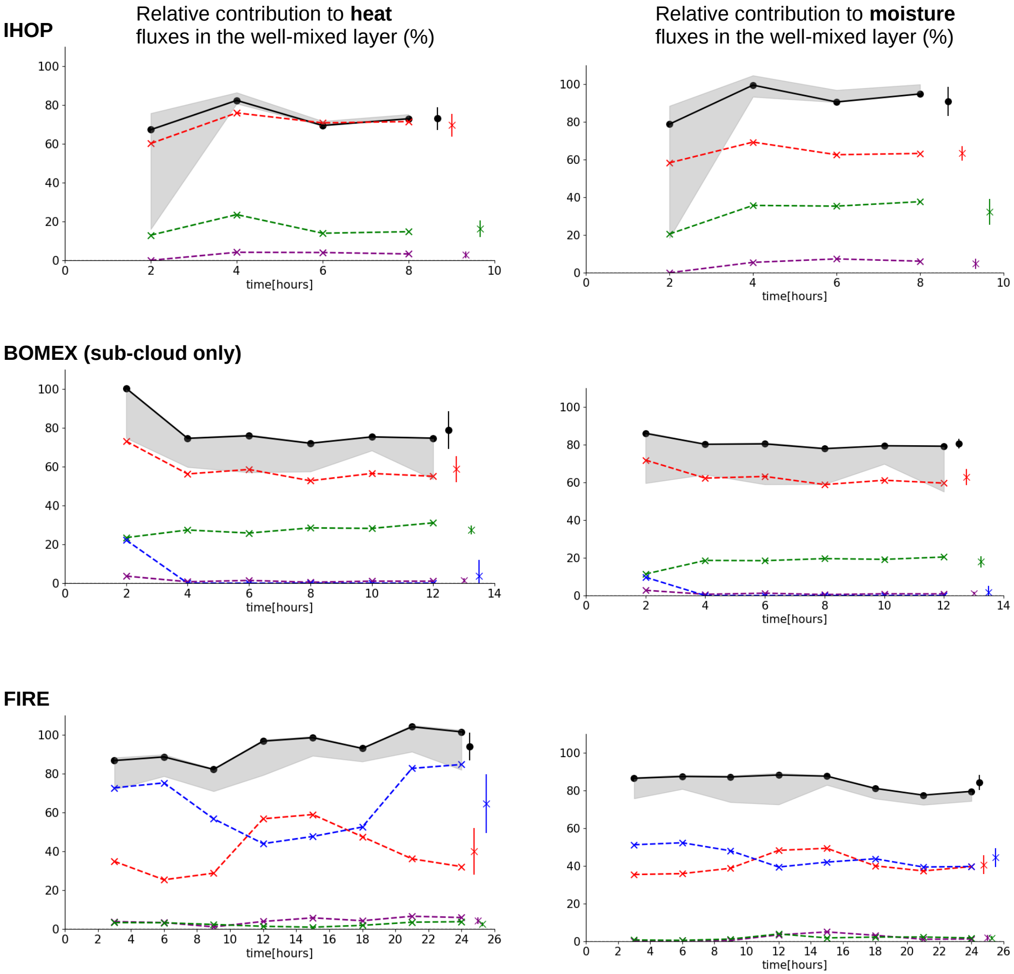

FIGURE 16 Vertically-averaged resolved fluxes of heat (left) and moisture (right) for IHOP (top), sub-cloud BOMEX (middle) and FIRE (bottom). Updraft, subsiding shells, sub-cloud downdraft and cloud-top downdrafts are represented as red, purple, green, and blue lines. Characteristics summed over all objects are represented with a black line for V_{min}=0.02 km^3, with the shaded grey area showing sensitivity of V_{min} ranged between 0.005 and 0.5 km^3.

Acknowledgements

This work received funding from grants HIGH-TUNE ANR-16-CE01-0010 and MOBYDYC ANR-22-CE01-0005. It was also supported by the DEPHY2 project, funded by the French national program LEFE/INSU and the GDR-DEPHY. The model is available on the Meso-NH website (`http://mesonh.aero.obs-mip.fr/`). Routines for the analysis of simulations and object identification are available on these Github (`https://github.com/florentbrient/objects-LES`) and Gitlab websites (`https://gitlab.com/tropics/objects/`) respectively.

references

Albright, A. L., B. Stevens, S. Bony, and R. Vogel (2023), A new conceptual picture of the trade wind transition layer, *J. Atmos. Sci.*, *80*(6), 1547–1563.

Bennett, L. J., T. M. Weckwerth, A. M. Blyth, B. Geerts, Q. Miao, and Y. P. Richardson (2010), Observations of the evolution of the nocturnal and convective boundary layers and the structure of open-celled convection on 14 june 2002, *Mon Weather Rev*, *138*(7), 2589–2607.

Bretherton, C. S., and M. Wyant (1997), Moisture transport, lower-tropospheric stability, and decoupling of cloud-topped boundary layers, *J. Atmos. Sci.*, *54*(1), 148–167.

Brient, F., F. Couvreux, N. Villefranque, C. Rio, and R. Honnert (2019), Object-oriented identification of coherent structures in large eddy simulations: Importance of downdrafts in stratocumulus, *Geophys Res Lett*, *46*(5), 2854–2864.

Caniaux, G., J. Redelsperger, and J. P. Lafore (1994), A numerical study of the stratiform region of a fast-moving squall line. part i: General description and water and heat budgets, *J. Atmos. Sci.*, *51*(14), 2046–2074.

Chinita, M. J., G. Matheou, and J. Teixeira (2018), A joint probability density–based decomposition of turbulence in the atmospheric boundary layer, *Mon Weather Rev*, *146*(2), 503–523.

Couston, L.-A., D. Lecoanet, B. Favier, and M. Le Bars (2017), Dynamics of mixed convective-stably-stratified fluids, *Phys. Rev. Fluids*, *2*(9), 094,804.

Couvreux, F., F. Guichard, J.-L. Redelsperger, C. Kiemle, V. Masson, J.-P. Lafore, and C. Flamant (2005), Water-vapour variability within a convective boundary-layer assessed by large-eddy simulations and ihop_2002 observations, *Quart. J. Roy. Meteor. Soc.*, *131*(611), 2665–2693.

Couvreux, F., F. Guichard, V. Masson, and J.-L. Redelsperger (2007), Negative water vapour skewness and dry tongues in the convective boundary layer: observations and large-eddy simulation budget analysis, *Bound. Lay. Meteor.*, *123*(2), 269–294.

Couvreux, F., F. Hourdin, and C. Rio (2010), Resolved versus parametrized boundary-layer plumes. part i: A parametrization-oriented conditional sampling in large-eddy simulations, *Bound. Lay. Meteor.*, *134*(3), 441–458.

Davini, P., F. D'Andrea, S.-B. Park, and P. Gentine (2017), Coherent structures in large-eddy simulations of a non-precipitating stratocumulus-topped boundary layer, *J. Atmos. Sci.*, (2017).

De Roode, S. R., I. Sandu, J. J. Van Der Dussen, A. S. Ackerman, P. Blossey, D. Jarecka, A. Lock, A. P. Siebesma, and B. Stevens (2016), Large-eddy simulations of euclipse–gass lagrangian stratocumulus-to-cumulus transitions: Mean state, turbulence, and decoupling, *J. Atmos. Sci.*, *73*(6), 2485–2508.

Deardorff, J. W. (1980), Stratocumulus-capped mixed layers derived from a three-dimensional model, *Boundary-Layer Meteorology*, *18*(4), 495–527.

Duynkerke, P. G., S. R. de Roode, M. C. van Zanten, J. Calvo, J. Cuxart, S. Cheinet, A. Chlond, H. Grenier, P. J. Jonker, M. Köhler, et al. (2004), Observations and numerical simulations of the diurnal cycle of the eurocs stratocumulus case, *Quart. J. Roy. Meteor. Soc.*, *130*(604), 3269–3296.

Feingold, G., I. Koren, H. Wang, H. Xue, and W. A. Brewer (2010), Precipitation-generated oscillations in open cellular cloud fields, *Nature*, *466*(7308), 849.

Geoffroy, O., J.-L. Brenguier, and F. Burnet (2010), Parametric representation of the cloud droplet spectra for les warm bulk microphysical schemes, *Atmos. Chem. Phys.*, *10*(10), 4835–4848.

Han, J., and C. S. Bretherton (2019), Tke-based moist eddy-diffusivity mass-flux (edmf) parameterization for vertical turbulent mixing, *Weather and Forecasting*, *34*(4), 869–886.

Heus, T., and H. J. Jonker (2008), Subsiding shells around shallow cumulus clouds, *Journal of the Atmospheric Sciences*, *65*(3), 1003–1018.

Hourdin, F., F. Couvreux, and L. Menut (2002), Parameterization of the dry convective boundary layer based on a mass flux representation of thermals, *J. Atmos. Sci.*, *59*(6), 1105–1123.

Hourdin, F., C. Rio, J.-Y. Grandpeix, J.-B. Madeleine, F. Cheruy, N. Rochetin, A. Jam, I. Musat, A. Idelkadi, L. Fairhead, et al. (2020), Lmdz6a: The atmospheric component of the ipsl climate model with improved and better tuned physics, *Journal of Advances in Modeling Earth Systems*, *12*(7), e2019MS001,892.

Jonas, P. (1990), Observations of cumulus cloud entrainment, *Atmospheric research*, *25*(1-3), 105–127.

Khairoutdinov, M., and Y. Kogan (2000), A new cloud physics parameterization in a large-eddy simulation model of marine stratocumulus, *Mon Weather Rev*, *128*(1), 229–243.

Lac, C., P. Chaboureau, V. Masson, P. Pinty, P. Tulet, J. Escobar, M. Leriche, C. Barthe, B. Aouizerats, C. Augros, et al. (2018), Overview of the meso-nh model version 5.4 and its applications, *Geosci. Model Dev. Discuss.*, pp. 1929–1969.

Lafore, J. P., J. Stein, N. Asencio, P. Bougeault, V. Ducrocq, J. Duron, C. Fischer, P. Héreil, P. Mascart, V. Masson, et al. (1998), The Meso-NH atmospheric simulation system. Part I: adiabatic formulation and control simulations, in *Ann. Geophys.*, vol. 16, pp. 90–109, Springer.

Lareau, N. P. (2020), Subcloud and cloud-base latent heat fluxes during shallow cumulus convection, *J. Atmos. Sci.*, *77*(3), 1081–1100.

Lareau, N. P., Y. Zhang, and S. A. Klein (2018), Observed boundary layer controls on shallow cumulus at the arm southern great plains site, *J. Atmos. Sci.*, *75*(7), 2235–2255.

Mahrt, L. (1991), Boundary-layer moisture regimes, *Quart. J. Roy. Meteor. Soc.*, *117*(497), 151–176.

Nicholls, S. (1989), The structure of radiatively driven convection in stratocumulus, *Quart. J. Roy. Meteor. Soc.*, *115*(487), 487–511.

Park, S.-B., P. Gentine, K. Schneider, and M. Farge (2016), Coherent structures in the boundary and cloud layers: Role of updrafts, subsiding shells, and environmental subsidence, *J. Atmos. Sci.*, *73*(4), 1789–1814.

Park, S.-B., T. Heus, and P. Gentine (2017), Role of convective mixing and evaporative cooling in shallow convection, *J. Geophys. Res.*, *122*(10), 5351–5363.

Pinty, J.-P., and P. Jabouille (1998), A mixed-phase cloud parameterization for use in mesoscale non-hydrostatic model: simulations of a squall line and of orographic precipitations, in *Conf. on Cloud Physics*, pp. 217–220, Amer. Meteor. Soc Everett, WA.

Randall, D. A. (1980), Entrainment into a stratocumulus layer with distributed radiative cooling, *J. Atmos. Sci.*, *37*(1), 148–159.

Richter, I. (2015), Climate model biases in the eastern tropical oceans: causes, impacts and ways forward, *Wiley Interdisciplinary Reviews: Climate Change*, *6*(3), 345–358.

Rio, C., and F. Hourdin (2008), A thermal plume model for the convective boundary layer: Representation of cumulus clouds, *Journal of the Atmospheric Sciences*, *65*(2), 407–425.

Romps, D. M., and A. B. Charn (2015), Sticky thermals: Evidence for a dominant balance between buoyancy and drag in cloud updrafts, *J. Atmos. Sci.*, *72*(8), 2890–2901.

Schmidt, H., and U. Schumann (1989), Coherent structure of the convective boundary layer derived from large-eddy simulations, *Journal of Fluid Mechanics*, *200*, 511–562.

Sherwood, S. C., D. Hernández-Deckers, M. Colin, and F. Robinson (2013), Slippery thermals and the cumulus entrainment paradox, *J. Atmos. Sci.*, *70*(8), 2426–2442.

Shipley, D., H. Weller, P. A. Clark, and W. A. McIntyre (2022), Two-fluid single-column modelling of rayleigh–bénard convection as a step towards multi-fluid modelling of atmospheric convection, *Quart. J. Roy. Meteor. Soc.*, *148*(742), 351–377.

Siebesma, A., and J. Cuijpers (1995), Evaluation of parametric assumptions for shallow cumulus convection, *J. Atmos. Sci.*, *52*(6), 650–666.

Siebesma, A.-P., C. Bretherton, A. Brown, A. Chlond, J. Cuxart, P. Duynkerke, H. Jiang, M. Khairoutdinov, D. Lewellen, C. Moeng, et al. (2003), A large eddy simulation intercomparison study of shallow cumulus convection, *J. Atmos. Sci.*, *60*(10), 1201–1219.

Siebesma, A. P., P. M. Soares, and J. Teixeira (2007), A combined eddy-diffusivity mass-flux approach for the convective boundary layer, *J. Atmos. Sci.*, *64*(4), 1230–1248.

Stevens, B., W. R. Cotton, G. Feingold, and C.-H. Moeng (1998), Large-eddy simulations of strongly precipitating, shallow, stratocumulus-topped boundary layers, *J. Atmos. Sci.*, *55*(24), 3616–3638.

Suselj, K., M. J. Kurowski, and J. Teixeira (2019), On the factors controlling the development of shallow convection in eddy-diffusivity/mass-flux models, *J. Atmos. Sci.*, *76*(2), 433–456.

Wang, S., and B. Stevens (2000), Top-hat representation of turbulence statistics in cloud-topped boundary layers: A large eddy simulation study, *J. Atmos. Sci.*, *57*(3), 423–441.

Williams, A., and J. Hacker (1993), Interactions between coherent eddies in the lower convective boundary layer, *Bound. Lay. Meteor.*, *64*, 55–74.

Willis, G., and J. Deardorff (1979), Laboratory observations of turbulent penetrative-convection planforms, *J. Geophys. Res.*, *84*(C1), 295–302.

Wood, R. (2012), Stratocumulus clouds, *Mon Weather Rev*, *140*(8), 2373–2423.

Wu, E., H. Yang, J. Kleissl, K. Suselj, M. J. Kurowski, and J. Teixeira (2020), On the parameterization of convective downdrafts for marine stratocumulus clouds, *Mon Weather Rev*, *148*(5), 1931–1950.

Yamaguchi, T., and D. A. Randall (2012), Cooling of entrained parcels in a large-eddy simulation, *J. Atmos. Sci.*, *69*(3), 1118–1136.

Zhou, X., and C. S. Bretherton (2019a), Simulation of mesoscale cellular convection in marine stratocumulus: 2. nondrizzling conditions, *J. Adv. Model. Earth Syst.*, *11*(1), 3–18.

Zhou, X., and C. S. Bretherton (2019b), The correlation of mesoscale humidity anomalies with mesoscale organization of marine stratocumulus from observations over the arm eastern north atlantic site, *J. Geophys. Res.*